

# unWISE tomography of Planck CMB lensing

Alex Krolewski<sup>b,c</sup> Simone Ferraro<sup>b</sup> Edward F. Schlafly<sup>b</sup> Martin White<sup>a,b,c</sup>

<sup>a</sup>Department of Physics, University of California, Berkeley, CA 94720

<sup>b</sup>Physics Division, Lawrence Berkeley National Laboratory, Berkeley, CA

<sup>c</sup>Department of Astronomy, University of California, Berkeley, CA 94720

E-mail: [krolewski@berkeley.edu](mailto:krolewski@berkeley.edu), [sferraro@lbl.gov](mailto:sferraro@lbl.gov), [eschlafly@lbl.gov](mailto:eschlafly@lbl.gov),  
[mwhite@berkeley.edu](mailto:mwhite@berkeley.edu)

**Abstract.** CMB lensing tomography, or the cross-correlation between CMB lensing maps and large-scale structure tracers over a well-defined redshift range, has the potential to map the amplitude and growth of structure over cosmic time, provide some of the most stringent tests of gravity, and break important degeneracies between cosmological parameters. In this work, we use the unWISE galaxy catalog to provide three samples at median redshifts  $z \sim 0.6, 1.1$  and  $1.5$ , fully spanning the Dark Energy dominated era, together with the most recent Planck CMB lensing maps. We obtain a combined cross-correlation significance  $S/N = 58.7$  over the range of scales  $300 < \ell < 1000$ . We measure the redshift distribution of unWISE sources by a combination of cross-matching with the COSMOS photometric catalog and cross-correlation with BOSS galaxies and quasars and eBOSS quasars. We also show that magnification bias must be included in our analysis and perform a number of null tests. In a companion paper, we explore the derived cosmological parameters by modeling the non-linearities and propagating the redshift distribution uncertainties.

**Keywords:** cosmological parameters from LSS – power spectrum – CMB – galaxy clustering

**ArXiv ePrint:** [19MM.NNNNN](https://arxiv.org/abs/19MM.NNNNN)

---

## Contents

|          |   |           |
|----------|---|-----------|
| <b>1</b> | <b>Introduction</b>   | <b>1</b>  |
| <b>2</b> | <b>The data</b>   | <b>2</b>  |
| 2.1      | Planck CMB lensing maps                                     | 2         |
| 2.2      | unWISE  | 3         |
| 2.3      | Galaxy selection  | 4         |
| 2.4      | Masks   | 5         |
| <b>3</b> | <b>Model</b>  | <b>6</b>  |
| 3.1      | Angular Clustering  | 6         |
| 3.2      | HaloFit model   | 7         |
| <b>4</b> | <b>Angular clustering</b>                                   | <b>8</b>  |
| 4.1      | Angular power spectra estimation                            | 8         |
| 4.2      | Covariance matrix   | 9         |
| <b>5</b> | <b>Galaxy redshift distribution</b>                         | <b>10</b> |
| 5.1      | Cross-match redshifts                                       | 10        |
| 5.2      | Cross-correlation redshifts                                 | 11        |
| 5.3      | Systematic errors in the cross-correlation $dN/dz$          | 17        |
| <b>6</b> | <b>Galaxy-lensing auto and cross-spectra</b>                | <b>20</b> |
| <b>7</b> | <b>Systematics in the cross-correlation and null tests</b>  | <b>21</b> |
| 7.1      | Stellar Contamination                                       | 21        |
| 7.2      | Foreground contamination to CMB lensing cross-correlations  | 22        |
| 7.3      | Galactic mask dependence of the sample properties           | 23        |
| 7.4      | Systematic uncertainties in the redshift distribution       | 25        |
| <b>8</b> | <b>Conclusions and lessons learned</b>                      | <b>26</b> |
| <b>A</b> | <b>Spectroscopic followup</b>                               | <b>28</b> |
| <b>B</b> | <b>Simple HOD model for unWISE samples</b>                  | <b>30</b> |
| <b>C</b> | <b>Response of the number density to magnification bias</b> | <b>36</b> |
| <b>D</b> | <b>Galaxy-galaxy cross spectra</b>                          | <b>37</b> |

---

## 1 Introduction

As they travel from the surface of last scattering to the Earth, Cosmic Microwave Background (CMB) photons are deflected by the gravitational potentials associated with large-scale structure (LSS), providing a probe of late-time physics directly in the CMB sky (see Refs. [1, 2] for reviews). The lensing effect is dominated by structures on Mpc scales over a very broad range

of redshifts from  $z < 1$  to  $z \sim 10$ . By cross-correlating the lensing map with another tracer of large-scale structure which spans a narrower range in redshift, we can simultaneously increase the signal-to-noise ratio and isolate particular redshifts of interest. Doing this on multiple lens redshift planes (“CMB lensing tomography”) breaks important degeneracies between the expansion history and the growth of perturbations, as well as providing greater control over systematics [3, 4]. The first detections of CMB lensing were obtained in cross-correlation between galaxy samples and WMAP data [5, 6], and some of the early work employing cross-correlations with ACT, SPT and Planck are presented in refs. [7–9] respectively. Since then, there have been a large number of cross-correlation analysis with a wide variety of samples (see for example refs. [10–16]).

In this work, we use galaxies from the unWISE catalog [17], containing angular positions and magnitudes of over two billion objects observed by the Wide-field Infrared Survey Explorer (WISE, [18]) mission. The unWISE catalog builds upon earlier WISE-based catalogs by including additional data from the post-hibernation NEOWISE mission, and is the largest full-sky galaxy catalog currently available [17], containing over half a billion galaxies across the full sky. We further divide the catalog based on magnitude and color and reject stars based on Gaia data [19], creating three samples, referred here as “blue”, “green” and “red,” at median redshifts  $\sim 0.6, 1.1$  and  $1.5$ , respectively, allowing a tomographic analysis of the amplitude of fluctuations in the Dark Energy dominated era. Previous cross-correlations between WISE-derived catalogs and CMB lensing were presented in refs. [9, 16, 20–23].

In this paper, we present the auto correlation of the galaxy samples and their cross-correlation with the Planck CMB lensing maps [24]. We also measure the redshift distribution of the unWISE galaxies, which is crucial for the cosmological interpretation of the signal. While obtaining photometric redshifts from the two WISE colors alone is not feasible, cross-matching sources with the COSMOS photometric catalog as well as cross correlation with a number of spectroscopic surveys allows us to determine the ensemble redshift distribution of our samples, together with an estimate of its uncertainty.

The outline of the paper is as follows: In Section 2 we summarize the data used and in Section 3 we describe our modelling. In Section 4 we discuss the auto and cross correlation measurements and in Section 5, we measure the redshift distribution of the unWISE sample and characterize its uncertainties. The results are presented in Section 6. Possible systematics and null tests are explored in Section 7, and in Section 8 we summarize our results. This paper is focused on the measurement of the cross-correlation. In a companion paper [25], we will extract cosmological information by modeling the non-linearities in the signal and marginalizing over uncertainties in the stellar contamination fraction and the galaxy redshift distribution.

Where necessary we assume a fiducial  $\Lambda$ CDM cosmology with the Planck 2018 maximum likelihood parameters (the final column in Table 2 in ref. [26]). We quote magnitudes in the Vega system, noting that we can easily convert these to AB magnitudes with  $AB = Vega + 2.699, 3.339$  in W1, W2, respectively.

## 2 The data

### 2.1 Planck CMB lensing maps

Gravitational lensing of the CMB remaps the temperature and polarization fields, altering their statistics in a well-defined way [1]. By searching for these statistical patterns it is possible to reconstruct the lensing convergence,  $\kappa$ , from quadratic combinations of the foreground-

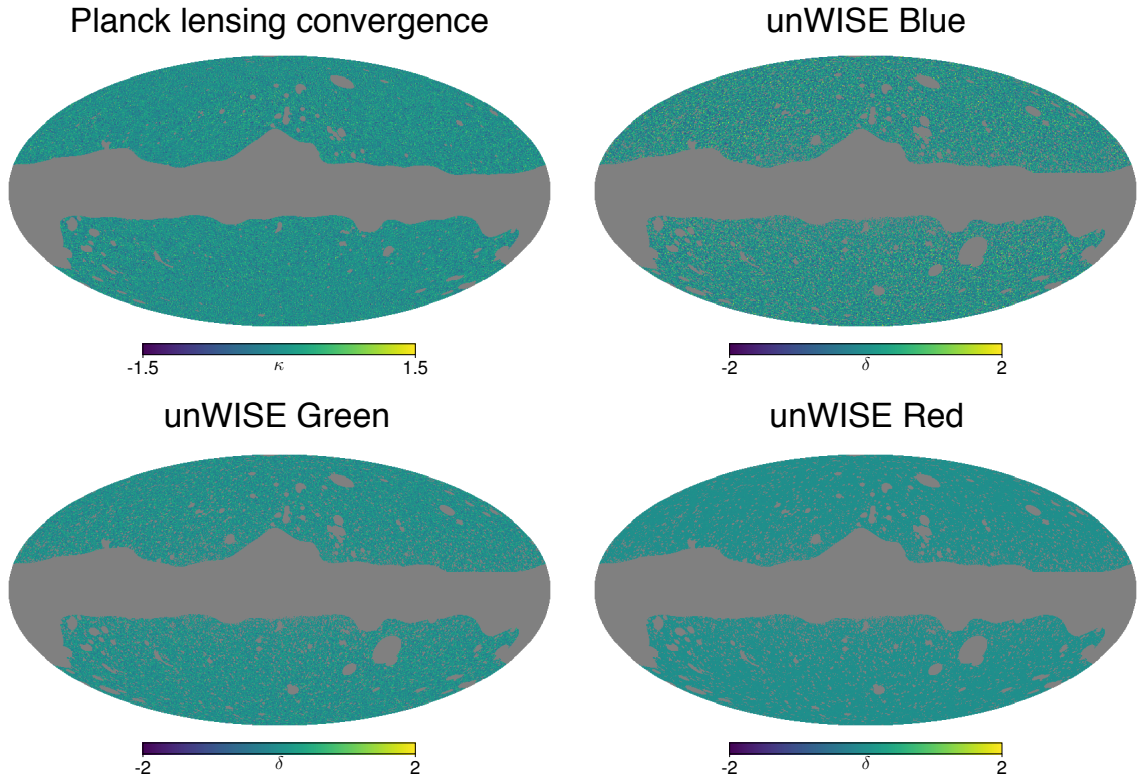


**Figure 1.** Plot of the maps used in the analysis ( $\kappa$  for Planck lensing convergence and density contrast  $\delta$  for the galaxy samples). The maps have been filtered to only contain the range of scales used in this analysis, i.e.  $\ell_{\min} = 100$  and  $\ell_{\max} = 1000$ , and this explains the lack of large-scale power.

cleaned maps [27]. We use the latest CMB lensing maps from the Planck 2018 release [24] and their associated masks, downloaded from the Planck Legacy Archive.<sup>1</sup> These maps are provided as spherical harmonic coefficients of the convergence,  $\kappa_{\ell m}$ , in HEALPix format [28] and with  $\ell_{\max} = 4096$ . In particular, for our fiducial analysis we use the minimum-variance (MV) estimate obtained from both temperature and polarization, based on the SMICA foreground-reduced CMB map. Since the MV reconstruction is dominated by temperature, residual galactic and extragalactic foregrounds may contaminate the signal. Extensive testing has been performed by the Planck team, indicating no significant problems at the current statistical level. Nonetheless, thermal Sunyaev-Zel’dovich (tSZ) contamination has been shown to be one of the largest potential contaminants to cross correlations with tracers of large-scale structure in other analyses [29–32]. For this reason, as a test, we shall repeat the analysis with a lensing reconstruction on SMICA foreground-reduced maps where tSZ has been explicitly deprojected [24], and we will refer to this analysis as “tSZ-free.” Possible foreground contamination is discussed more in detail in Section 7.2.

## 2.2 unWISE

The WISE mission mapped the entire sky at 3.4, 4.6, 12, and 22  $\mu\text{m}$  (W1, W2, W3, and W4) with angular resolutions of 6.1”, 6.4”, 6.5” and 12”, respectively [18]. The AllWISE data

<sup>1</sup>PLA: <https://pla.esac.esa.int/>

| Label | $W1 - W2 > x$       | $W1 - W2 < x$       | $W2 < x$ | $\bar{z}$ | $\delta z$ | $\bar{n}$ | $s$   |
|-------|---------------------|---------------------|----------|-----------|------------|-----------|-------|
| Blue  |                     | $(17 - W2)/4 + 0.3$ | 16.7     | 0.6       | 0.3        | 3409      | 0.455 |
| Green | $(17 - W2)/4 + 0.3$ | $(17 - W2)/4 + 0.8$ | 16.7     | 1.1       | 0.4        | 1846      | 0.648 |
| Red   | $(17 - W2)/4 + 0.8$ |                     | 16.2     | 1.5       | 0.4        | 144       | 0.842 |

**Table 1.** Color and magnitude cuts for selecting galaxies of different redshifts, together with the mean redshift,  $\bar{z}$ , and the width of the redshift distribution,  $\delta z$  (as measured by matching to objects with photometric redshifts on the COSMOS field [40]), number density per  $\text{deg}^2$  within the unWISE mask,  $\bar{n}$ , and response of the number density to magnification,  $s \equiv d \log_{10} N/dm$ . Galaxies are additionally required to have  $W2 > 15.5$ , to be undetected or not pointlike in Gaia (see §2.3), and to not be flagged as diffraction spikes, latents or ghosts.  $s$  is measured using galaxies at ecliptic latitude  $|\lambda| > 60^\circ$ , where WISE reaches fainter limiting magnitudes due to increased depth of coverage (see Appendix C).

release encompassed the full WISE cryogenic mission as well as the initial NEOWISE post-cryogenic mission, from 2010 January to 2011 February, after which the instrument was placed into hibernation [33, 34]. The W1 and W2 bands do not require cryogen to operate efficiently, motivating reactivation of WISE in December 2013 [35]. Observations from the continuing NEOWISE mission have been incorporated into increasingly deep “unWISE” coadded images of the sky [36–38], which now feature more than  $4\times$  longer exposure times than were available for the AllWISE data release. In the future, at least another two years of NEOWISE data will be available (NEO5 and NEO6), which would further increase the depth by  $\sim 0.2$  magnitudes.

The deeper imaging coupled with the  $\sim 6.5''$  angular resolution leads to crowded images with many overlapping sources, requiring a new approach to the analysis of the WISE coadded images. The `crowdsourc` crowded field photometry pipeline [39], originally designed for surveys of the Galactic plane, was employed to generate a new catalog based on the deep unWISE coadded images [17]. The resulting catalog provides a sample of  $> 500$  million galaxies with  $0 < z < 2$  and improves the uniformity of the depth and photometric calibration of the WISE survey.

### 2.3 Galaxy selection

Galaxies are selected on the basis of their WISE W1 and W2 magnitudes. Inspection of the average colors of galaxies detected in WISE as a function of redshift shows a clear trend in which fainter and redder galaxies tend to be at higher redshift. Accordingly we made three selections of galaxies in  $W1 - W2$  color, with a sliding cut on color with magnitude reflecting that fainter galaxies tend to be at higher redshifts. Table 1 gives the adopted color selection for the three samples considered in this work, which we term the blue, green, and red samples [17]. Table 1 also summarizes important properties of each sample including the redshift distribution, the number density, and the response of number density to galaxy magnification  $s \equiv d \log_{10} N/dm$ . We measure  $s$  using galaxies with ecliptic latitude  $|\lambda| > 60^\circ$ , where the WISE depth of coverage is greater and thus the measurement of  $s$  is less affected by incompleteness. We describe the measurement of  $s$  in Appendix C.

We require that the blue and green samples have  $15.5 < W2 < 16.7$ , and the red sample has  $15.5 < W2 < 16.2$ . If we allow the red sample to include sources with  $16.2 < W2 < 16.7$ , we find that the red-blue cross-correlation is inconsistent at the  $2\text{-}3\sigma$  level with the expected cross-correlation given the bias measured from the CMB-cross spectra (Appendix D). The fainter red samples also exhibit a decrease in number density closer to the Galactic plane, and may have more angular variation in  $dN/dz$ . As a result, we suspect that the fainter

red sample is more affected by stellar contamination or systematics-driven fluctuations, and exclude it from our fiducial definition of the red sample.

Each of the samples is required to be either undetected or not pointlike in Gaia. Here a source is taken as “pointlike” if

$$\text{pointlike}(G, A) = \begin{cases} \log_{10} A < 0.5 & \text{if } G < 19.25 \\ \log_{10} A < 0.5 + \frac{5}{16}(G - 19.25) & \text{otherwise,} \end{cases} \quad (2.1)$$

where  $G$  is the Gaia  $G$  band magnitude and  $A$  is `astrometric_excess_noise` from Gaia DR2 [41]. A source is considered “undetected” in Gaia if there is no Gaia DR2 source within  $2.75''$  of the location of the WISE source. High `astrometric_excess_noise` indicates that the Gaia astrometry of a source was more uncertain than typical for resolved sources; this cut essentially takes advantage of the  $0.1''$  angular resolution of Gaia to morphologically separate point sources from galaxies. We additionally remove sources classified as diffraction spikes, first or second latents, or ghosts in either W1 or W2, corresponding to “unWISE flags” 1, 2, 3, 4 or 7.<sup>2</sup>

## 2.4 Masks

For the lensing map, we use the official 2018 Planck lensing mask, provided together with the other data products [24]. This is created using a combination of the SMICA 70% Galactic mask, retaining the cleanest 70% of the sky, together with the 143 and 217 GHz point source masks and the tSZ-detected clusters with  $S/N > 5$  [24]. We additionally masked a small region of the sky unmasked in the Planck map with  $|b| < 10^\circ$ . Overall, this leaves an unmasked sky fraction  $f_{\text{sky}} = 0.670$  for the lensing map. As a test of Galactic contamination we also use the 60 and 40% temperature masks from the Planck 2018 data release<sup>3</sup>, masking an increasing fraction of the Galactic plane. The impact on the results is discussed in Section 7.3.

For WISE, we found it convenient to use the Planck lensing mask as an effective galactic mask, to avoid excessive stellar contamination close to the galactic plane. We additionally mask stars, galaxies, planetary nebulae, and `NSIDE = 2048` HEALPix pixels with substantial area lost due to sub-pixel unWISE masks (e.g. for diffraction spikes from bright stars).

We mask the 6678 brightest stars in the infrared sky (6156 at  $|b| > 20^\circ$ ) with  $W1 < 2.5$  or  $W2 < 2$  or  $K < 2$  (where the WISE magnitude is the brighter of the AllWISE or unWISE magnitudes). We use the bright star list provided by the CatWISE team (Eisenhardt et al., in prep)<sup>4</sup> for these objects.<sup>5</sup> We find that a disk of radius  $0.5^\circ$  is adequate to prevent contamination due to spurious detections around the majority of these bright sources. For the very brightest stars, diffraction spikes extend beyond the  $\sim 1^\circ$  extent of the diffraction spike mask; we therefore use a  $1.5^\circ$  radius around 32 stars with  $-3 < W2 < -2$  and a  $3^\circ$  radius around 11 stars with  $W2 < -3$ . Finally, we mask  $0.2^\circ$  around 6212 stars with  $2 < W2 < 2.5$ ,  $W1 > 2.5$ , and  $K > 2$ , where we find that in rare cases, the unWISE PSF model does not extend far enough into the wings of the star, leading to spurious sources at the edge of the modeled region.

<sup>2</sup>See Table 5 here: [http://catalog.unwise.me/files/unwise\\_bitmask\\_writeup-03Dec2018.pdf](http://catalog.unwise.me/files/unwise_bitmask_writeup-03Dec2018.pdf)

<sup>3</sup>Always multiplied by the original lensing mask.

<sup>4</sup>[catwise.github.io](http://catwise.github.io)

<sup>5</sup>We additionally add the carbon star IRC+20326, which had problematic photometry in both AllWISE and unWISE.

We also mask bright galaxies using the LSLGA catalog<sup>6</sup>, selecting 715 galaxies from Hyperleda [42] with magnitudes  $< 13$  (almost always in the  $B$  filter, though in rare cases the  $K$  or  $I$  filter), diameter  $D_{25} > 3$  arcmin, and surface brightness within  $D_{25}$  of  $< 26$  mag/arcsec<sup>2</sup>. Using the position angle and ellipticity in the catalog we mask ellipses around each galaxy out to  $1.5R_{25}$ , and we visually confirm that this radius removes the impact of galaxies on our samples.

We also find that planetary nebulae can contaminate our samples, particularly the red sample. We mask 1143 planetary nebulae [43], masking out to twice the optical radius of each planetary nebula.

In all three cases (stars, galaxies, and planetary nebulae) we create a binary mask on an NSIDE = 2048 HEALPix map, masking all pixels within the specified distance of the source. For the planetary nebulae, we additionally use the “inclusive=True” option in the HEALPix QUERY\_DISC command since the pixels in our map are often larger than the mask radius.

Finally, we correct for area lost in each (NSIDE = 2048) HEALPix pixel from sub-pixel masking. Sub-pixel masking arises from two sources: foreground Galactic stars from Gaia, which will mask any unWISE source within  $2.75''$  due to our Gaia point-source exclusion, and unWISE masking of diffraction spikes, latents and ghosts around bright stars<sup>7</sup>. We apply a binary mask to remove all pixels with more than 20% area lost due to sub-pixel masking, and we correct the density in the remaining pixels by dividing by the fractional unmasked area of each pixel.

We apodize the Planck lensing mask (with additional exclusion of  $|b| < 10^\circ$ ) with a  $1^\circ$  FWHM Gaussian. We do not apodize the stellar, large galaxy, planetary nebulae or area lost masks. We use the apodized Planck lensing mask for the CMB lensing map and the product of the apodized lensing mask and the unapodized stellar, large galaxy, planetary nebulae and area-lost masks for the unWISE galaxy map. This yields  $f_{\text{sky}} = 0.586$  for the unWISE galaxy map.

### 3 Model

#### 3.1 Angular Clustering

Both the CMB lensing convergence  $\kappa$  and the unWISE projected galaxy density are projections of 3D density fields. We define the projection through kernels  $W(\chi)$ , where  $\chi$  is the line-of-sight comoving distance. Given two such fields  $X, Y$  on the sky their angular cross-power spectrum is

$$C_\ell^{XY} = \frac{2}{\pi} \int_0^\infty d\chi_1 d\chi_2 W^X(\chi_1) W^Y(\chi_2) \int_0^\infty k^2 dk P_{XY}(k; z_1, z_2) j_\ell(k\chi_1) j_\ell(k\chi_2) \quad . \quad (3.1)$$

On small angular scales (high  $\ell$ ) one may make the Limber approximation [44], under which  $C_\ell$  reduces to a single integral of the equal-time, real-space power spectrum:

$$C_\ell^{XY} = \int d\chi \frac{W^X(\chi) W^Y(\chi)}{\chi^2} P_{XY} \left( k_\perp = \frac{\ell + 1/2}{\chi}, k_z = 0 \right) \quad (3.2)$$

where we have included the lowest order correction to the Limber approximation,  $\ell \rightarrow \ell + 1/2$ , to increase the accuracy to  $\mathcal{O}(\ell^{-2})$  [45].

<sup>6</sup><https://github.com/moustakas/LSLGA>

<sup>7</sup>[http://catalog.unwise.me/files/unwise\\_bitmask\\_writeup-03Dec2018.pdf](http://catalog.unwise.me/files/unwise_bitmask_writeup-03Dec2018.pdf)

Lensing is sourced by the Weyl potential, which is related to the total matter power spectrum (including neutrinos) by the Poisson equation. Writing  $C_\ell$  in terms of the galaxy-matter and matter-matter power spectra  $P_{\text{mg}}$  and  $P_{\text{gg}}$ , the weight functions  $W(\chi)$  are

$$W^\kappa(\chi) = \frac{3}{2}(\Omega_m + \Omega_\nu)H_0^2(1+z) \frac{\chi(\chi_\star - \chi)}{\chi_\star} \quad , \quad W^g(\chi) = b(z)H(z) \frac{dN}{dz} \quad (3.3)$$

with  $\chi_\star$  the distance to last scattering and  $\int dz dN/dz = 1$ .

Besides density-density and density-lensing correlations, there are also correlations induced by lensing magnification of background sources:

$$C_\ell^{\kappa g} \rightarrow C_\ell^{\kappa g} + C_\ell^{\kappa \mu} \quad (3.4)$$

$$C_\ell^{g_1 g_2} \rightarrow C_\ell^{g_1 g_2} + C_\ell^{g_1 \mu_2} + C_\ell^{g_2 \mu_1} + C_\ell^{\mu_1 \mu_2} \quad (3.5)$$

where

$$W^{\mu, i}(\chi) = (5s - 2) \frac{3}{2}(\Omega_m + \Omega_\nu)H_0^2(1+z)g_i(\chi) \quad (3.6)$$

$$g_i(\chi) = \int_\chi^{\chi_\star} d\chi' \frac{\chi(\chi' - \chi)}{\chi'} H(z') \frac{dN_i}{dz'} \quad (3.7)$$

where  $s \equiv d \log_{10} N/dm$  is the response of the number density to a multiplicative change in brightness. Given our complex selection function, we measure the response by finite difference, artificially changing each magnitude by the same amount (in analogy to lensing magnification) and measuring the change in number of galaxies satisfying our selection criteria. This procedure is discussed in detail in Appendix C for both the unWISE galaxies (necessary for modeling the angular power spectra) and for the spectroscopic samples (necessary for determining magnification bias contamination to the clustering redshifts). For the color-selected unWISE samples, the response  $s$  may be significantly different from the slope of the luminosity function at the magnitude limit because the color cut is magnitude dependent.

### 3.2 HaloFit model

In order to compute  $C_\ell$  we need to model  $P_{\text{gg}}(k, z)$ ,  $P_{\text{mg}}(k, z)$  and  $P_{\text{mm}}(k, z)$ . In this paper, we do not explore the cosmological implications of our measurement, but rather seek to characterize the unWISE samples and their redshift distribution, and present a measurement of the cross-correlations. For this purpose, a phenomenological fit will be sufficient, and we choose to model the auto and cross correlation in terms of a linear bias, multiplied by the ‘‘HaloFit’’ fitting function [46] to the non-linear matter power spectrum as implemented in the CLASS code [47]:

$$P_{\text{mg}}(k, z) = b_{\text{lin}}(z)P_{\text{mm}}(k, z) \quad , \quad P_{\text{gg}}(k, z) = b_{\text{lin}}^2(z)P_{\text{mm}}(k, z) + \text{Shot Noise} \quad (3.8)$$

This procedure has been shown to produce fairly reasonable phenomenological fits to the auto and cross correlations.<sup>8</sup> While the fit may be good, ref. [48] has shown that the value of the inferred cosmological parameters can be significantly biased if HaloFit is used, and for this reason we will explore a more sophisticated bias model to better model non-linearities in our cosmological analysis in ref. [25].

<sup>8</sup>For the magnification bias terms, each  $\ell$  maps to higher  $k$  than for the clustering terms; therefore the linear bias times HaloFit model is less adequate for  $C_\ell^{\mu g}$ . However, the magnification bias terms are subdominant compared to the clustering terms, so inaccuracy in modeling  $C_\ell^{\mu g}$  is not significant.

Since the galaxy field responds to dark matter and baryons only [49–53],  $P_{\text{gg}}$  is the power spectrum of non-neutrino density fluctuations. Although lensing responds to the power spectrum of total fluctuations, on the scales of interest here the neutrinos cause a scale-independent suppression of power. Therefore, using the non-neutrino power spectrum throughout and substituting  $\Omega_m + \Omega_\nu \rightarrow \Omega_m$  greatly simplifies the modelling and makes less than 1% difference compared to the exact calculation.

## 4 Angular clustering

In this section we discuss our method of estimating the auto and cross spectra, as well as their covariance matrix.

### 4.1 Angular power spectra estimation

In order to estimate the binned cross and auto power spectra, we use a pseudo- $C_\ell$  estimator [54] based on the harmonic coefficients of the galaxy and lensing fields. The measured pseudo- $C_\ell$  on the cut sky are calculated as

$$\tilde{C}_\ell^{XY} = \frac{1}{2\ell + 1} \sum_m X_{\ell m} Y_{\ell m}^* \quad (4.1)$$

where  $X, Y \in \{g_1, g_2, g_3, \kappa\}$  are the observed fields on the cut sky. Because of the mask, these differ from the true  $C_\ell$  that are calculated from theory, but their expectation value is related through a mode-coupling matrix,  $M_{\ell\ell'}$ , such that

$$\langle \tilde{C}_\ell \rangle = \sum_{\ell'} M_{\ell\ell'} C_{\ell'} \quad (4.2)$$

The matrix  $M_{\ell\ell'}$  is purely geometric and can be computed from the power spectrum of the mask itself. While Eq. (4.2) is not directly invertible for all  $\ell$ , the MASTER algorithm [54] provides an efficient method to do so assuming that the power spectrum is piecewise constant in a number of discrete bins,  $b$ . Defining a “binned” mode-coupling matrix,  $\mathcal{M}_{bb'}$  [55], we can recover unbiased binned bandpowers

$$C_b = \sum_{b'} \mathcal{M}_{bb'}^{-1} \tilde{C}_{b'} \quad . \quad (4.3)$$

We use the implementation in the code `NaMaster`<sup>9</sup> [55]. Finally, the theory curve must be binned in the same way as the data when comparing theory and measurements. Since the true  $C_\ell$  are not piecewise constant, this involves the following steps [55]: First, the theory curve is convolved with  $M_{\ell\ell'}$  using Eq. (4.2). Then the convolved theory,  $\tilde{C}_\ell^{\text{theory}}$ , is binned in the same bins,  $b$ , as the data to form bandpowers,  $\tilde{C}_b^{\text{theory}}$ , and finally the bandpowers are decoupled using Eq. (4.3) to obtain  $C_b^{\text{theory}}$ . While for simplicity the plots show unbinned theory curves, all of the calculations are performed with binned quantities.

In short, our pipeline works as follows: first, we mask the Planck lensing map with the mask provided by the Planck team, apodized with a Gaussian smoothing kernel with FWHM 1 deg. For the unWISE galaxies, we use the custom-made mask described in Section 2.4, which includes different apodization schemes for the wide Galactic mask and point sources.

<sup>9</sup><https://github.com/LSSDESC/NaMaster>

In addition, we have to consider that Galactic stars can mask galaxies behind them or in their vicinity, a problem that becomes more severe closer to the galactic plane. To correct for this, we create an “area lost” mask (described in Section 2.4) and divide the observed galaxy number count by the area available in each pixel, to obtain an unbiased estimate of the local number of galaxies. Then a galaxy overdensity field is created, and cross-correlated with the CMB lensing maps using **NaMaster**. Finally, we need to correct for the pixel window function, due to the assignment of galaxies to discrete pixels: we divide  $C_\ell^{kg}$  by the HEALPix pixel window function at the center of each bandpower, and  $C_\ell^{gg}$  by the square of the pixel window function.

We tested this pipeline on Gaussian realizations of the CMB lensing and galaxy fields, and noted that the final “deconvolved”  $C_\ell$  are rather sensitive to the choice of apodization scale, especially for the CMB lensing map, but are not affected by the inclusion of unapodized components in the galaxy mask. Our choice of smoothing was determined by optimizing the recovered power spectrum in simulations with known input angular correlation. In particular, we use the above **NaMaster** pipeline to measure  $C_\ell$  for 100 simulated Gaussian lensing and galaxy maps (generated with the correct cross-correlation). We find significant biases due to power leakage outside the measured range, if the  $\ell_{\max}^{\text{NaMaster}}$  used in **NaMaster** is close to the  $\ell_{\max} = 1000$  used in our analysis. To remedy this, we run **NaMaster** with  $\ell_{\max}^{\text{NaMaster}} = 6000$ , before extracting the bandpowers in our analysis range and discarding the higher  $\ell$  ones. With this choice, we have confirmed that all of the auto- and cross-correlations are recovered to better than 0.5% in every bandpower.

One further concern is that the measured  $C_\ell^{gg}$  at  $\ell < 200$ , which is not used in our analysis, is considerably larger than the theory prediction for galaxy clustering, which we use above to create Gaussian realizations to test our pipeline. This is likely due to large-scale systematics and stellar contamination in the unWISE dataset, and the mask-induced mode coupling could potentially create a leakage of extra power into the bandpowers used in the analysis. To test for this, we replace our best-fit  $C_\ell^{gg}$  theory curve at  $\ell \lesssim 200$  with a piecewise function approximately representing the sharp low- $\ell$  rise in the galaxy auto-spectrum in the Gaussian pipeline test above, and we find that the recovered bandpowers at  $300 < \ell < 1000$  change by less than 0.2%.

We conclude that with our pipeline we can measure all of the auto and cross-correlations between the different samples with sub-percent accuracy over the whole range of scales considered.

## 4.2 Covariance matrix

While an exact computation of the covariance matrix after applying the MASTER algorithm for a Gaussian random field is possible, it is computationally very demanding, involving  $\mathcal{O}(\ell_{\max}^6)$  operations. Refs. [56, 57] have proposed an approximate method to estimate the Gaussian part of the covariance matrix that makes it as computationally expensive as the power spectrum itself. This procedure has been validated on simulations and shown to work extremely well [57]. This algorithm is implemented in **NaMaster**, and takes as input the true auto and cross spectra (for example, from the theory curves with the correct value of parameters including the galaxy bias). Since measuring the bias requires a covariance matrix to start with, an iterative approach may be used. For computational simplicity, we adopt a further approximation which will assume the decoupled covariance matrix to be diagonal,

and where the on-diagonal elements for binned bandpowers of width  $\Delta\ell$  are given by [54]:

$$\text{Cov}(C_\ell^{XY}, C_{\ell'}^{XY}) = \sigma^2(C_\ell^{XY})\delta_{\ell,\ell'} = \frac{[C_\ell^{XX}C_\ell^{YY} + (C_\ell^{XY})^2]_{\text{measured}}}{f_{\text{sky}}(2\ell + 1)\Delta\ell} \frac{w_4}{w_2^2} \delta_{\ell,\ell'} \quad (4.4)$$

Here the weights  $w_2$  and  $w_4$  are defined in terms of the arbitrary mask weights  $W(\hat{\mathbf{n}})$  as:

$$w_i f_{\text{sky}} = \frac{1}{4\pi} \int_{4\pi} d\Omega_{\hat{\mathbf{n}}} W^i(\hat{\mathbf{n}}) \quad (4.5)$$

with  $w_1 f_{\text{sky}} = f_{\text{sky}}$ . If  $X \neq Y$  and the fields have different masks, we take  $w_2$  and  $w_4$  to be the geometric means of the ones computed with each of the individual masks.

Using the method in refs. [56, 57], we have checked that the largest off-diagonal correlation between bandpowers is 4% for the two lowest  $\ell$  bins, and that the on-diagonal elements agree to percent level. Therefore we conclude that the approximation in Equation 4.4 is adequate for our purposes. Furthermore, we neglect any non-Gaussian contribution to the covariance matrix, since we will only model scales that are in the linear or mildly non-linear regimes, where these corrections are expected to be small.

## 5 Galaxy redshift distribution

Since the unWISE galaxy sample is selected from two-band imaging,  $dN/dz$  cannot be determined by photometric redshifts. We instead measure  $dN/dz$  using cross-correlations with large-area spectroscopic surveys [58–60], supplemented by redshifts from cross-matching to deep photometric surveys across small areas of the sky. Cross-correlation redshifts measure  $b(z)dN/dz$  (in the absence of a small contribution from magnification bias), which is the relevant kernel for modeling  $C_\ell^{\kappa g}$  and  $C_\ell^{gg}$  (Section 3). Therefore, unlike previous work, we are not concerned with disentangling  $dN/dz$  from the bias evolution of the unWISE galaxies.  $C_\ell^{\kappa g}$  and  $C_\ell^{gg}$  do contain a subdominant contribution from magnification bias, which depends on  $dN/dz$  alone; in this context, we use  $dN/dz$  measured from cross matches to the COSMOS photometric catalog. In Appendix B we show that this approach is self-consistent: modeling the spectroscopic cross-correlations with the cross-match  $dN/dz$  yields an unWISE bias evolution consistent with a simple halo occupation distribution of the unWISE galaxies (Figure 16). In Sections 5.1 and 5.2 we describe our methodology for measuring the cross-correlation and cross-match redshifts and estimating their uncertainties, which constitute a substantial portion of the error budget in modeling the angular power spectra.

### 5.1 Cross-match redshifts

One estimate of  $dN/dz$  can be obtained by matching the unWISE samples to deep catalogs with photometric redshifts. The deepest sample of well-measured photometric redshifts comes from the COSMOS field, where deep photometry in many bands spanning the ultraviolet through infrared allows precise photometric redshifts for all sources detected by WISE with  $\Delta z/(1+z) = 0.007$  [40]. We first trim the COSMOS catalog to include only objects brighter than 20.7 (19.2) Vega mag at 3.6 (4.2)  $\mu\text{m}$ . These depths are roughly 2.5 mag fainter than the 50% completeness limit for the unWISE catalog [17], so excluding fainter objects removes no objects that WISE could conceivably detect. We then match COSMOS sources to unWISE sources at a radius of 2.75'' over the 2 deg<sup>2</sup> overlap, considering the closest COSMOS source within 2.75'' to be the true match.

The COSMOS catalog marks many bright stars as galaxies, so we additionally edit the COSMOS catalog so that bright objects which Gaia identifies as pointlike are classified as stars, as long as those objects are not X-ray selected. We find that stellar contamination of the unWISE samples is very low, with 1.8%, 1.6%, and likely  $< 1\%$ <sup>10</sup> of the blue, green and red samples classified as stars.

For each source, we use the redshift corresponding to the median of the likelihood distribution (“photoz” in the COSMOS catalog). If the SED is better fit by an AGN template than a galaxy template, we instead use the redshift from the AGN template fit (“zq” in the catalog); we find 19%, 30% and 41% of the blue, green and red sample are classified as AGN by this criterion. However, for these objects “zq” and “photoz” are very similar.

Due to the small area of the COSMOS field, sample variance can be larger than the Poisson variance on  $dN/dz$ . We therefore estimate uncertainty on  $dN/dz$  by constructing 44 subsamples, each of  $\sim 2 \text{ deg}^2$ , from the HSC SSP survey [61, 62]. Compared to COSMOS, HSC is slightly shallower but covers a much larger area ( $\sim 120 \text{ deg}^2$ ). However, the HSC photometric redshifts are less accurate than COSMOS and become biased at  $z > 1.5$ ,<sup>11</sup> where a substantial fraction of galaxies scatter to  $z_{\text{HSC}} \sim 1$ , biasing  $dN/dz_{\text{HSC}}$  at  $z \geq 1$  compared to  $dN/dz_{\text{COSMOS}}$ . As a result, we restrict the HSC comparison to  $z < 1$ . We use the DEmP photometric redshifts, as these are the most accurate redshifts available for all “primary” HSC objects [62]. We require that the HSC objects have clean photometry: we only use “primary” sources, and remove sources with pixel flags indicating saturated or interpolated pixels, bad pixels, cosmic ray hits, suspect and clipped pixels, and poor centroid measurements. We also require that the objects are classified as extended sources or have  $i > 23$ , where the star-galaxy classification performs poorly. As with COSMOS, we use the closest match within  $2.75''$ .

We find that the  $dN/dz$  errors are larger than Poisson statistics would indicate, by roughly redshift-independent factors of 3.8, 1.9 and 1.1 for the blue, green and red samples at  $z < 1$ . Since we cannot use HSC to determine  $dN/dz$  errors at  $z > 1$ , where the DEmP photometric redshifts become significantly biased, we extrapolate the  $dN/dz$  uncertainty to higher redshift by multiplying the Poisson error bars by a constant factor of 3.8, 1.9 and 1.1 for blue, green and red samples. We give summary statistics for the cross-match  $dN/dz$  in Table 3 and plot the cross-match  $dN/dz$  in Figure 5.

## 5.2 Cross-correlation redshifts

Another method for determining  $dN/dz$  is through cross-correlation with a spectroscopic sample. This is an old method has been revived in several recent works [58–60, 63–74], but here we present one of its first applications to modeling galaxy power spectra. We therefore discuss and quantify several sources of systematic error, including nonlinear clustering and nonlinear bias evolution; magnification bias contribution to the photometric-spectroscopic cross-correlation; and bias evolution of the various spectroscopic samples as required to combine cross-correlations with multiple spectroscopic samples.

In the Limber approximation the cross-correlation of a photometric survey with scale-independent bias  $b_{\text{sml,p}}(z)$  and redshift distribution  $dN_{\text{p}}/dz$ , and a spectroscopic survey with

<sup>10</sup>The red sample only has 188 matches to the COSMOS photometric catalog and none of them are stars; the error on the stellar contamination fraction may therefore be quite large. For the fainter red samples reaching to  $W2 = 16.5$  or  $16.7$ , we find stellar contamination of 0.6% and 0.8%, respectively.

<sup>11</sup>See page A5 in [https://hsc-release.mtk.nao.ac.jp/doc/wp-content/uploads/2017/02/s16a\\_demp\\_median.pdf](https://hsc-release.mtk.nao.ac.jp/doc/wp-content/uploads/2017/02/s16a_demp_median.pdf), which plots bias, scatter, and outlier fraction as a function of reference redshift for the training set used by HSC.

bias  $b_{\text{sml},s}(z)$ , in a narrow bin between  $z_{\text{min}}$  and  $z_{\text{max}}$  is

$$C_\ell^{\text{p-s cross}} = b_{\text{sml},s}(z) b_{\text{sml},p}(z) H(z) \frac{dN_p}{dz} \int_{z_{\text{min}}}^{z_{\text{max}}} dz \frac{dN_s}{dz} \frac{P_{\text{mm}}(k = (\ell + \frac{1}{2})/\chi, z)}{\chi^2} + C_\ell^{\text{mag}} \quad (5.1)$$

where  $C_\ell^{\text{mag}}$  includes the contributions from the three lensing magnification bias terms; we assume the bin is sufficiently narrow that the biases and  $dN_p/d\chi$  are constant across the bin; and both biases are assumed to be scale-independent.

We refer to the biases here as  $b_{\text{sml}}$  to emphasize that they are defined on relatively small scales ( $2.5 - 10 h^{-1}$  Mpc) on which we measure the spectroscopic-photometric cross-correlations. This is in contrast to the large-scale bias,  $b_{\text{lin}}$ , relevant to the modeling of the angular power spectrum in Section 3. However, as discussed below and in Section 7,  $b_{\text{sml}}$  and  $b_{\text{lin}}$  are within 15% of each other for all of the unWISE samples, and the systematic error from the discrepancy between  $b_{\text{sml}}$  and  $b_{\text{lin}}$  is subdominant to the statistical error from uncertainty in  $b dN/dz$ .

We have implemented a cross-correlation  $dN/dz$  estimate in both harmonic and configuration space, obtaining consistent results. It is convenient, and consistent with past results, to first present the spectroscopic-photometric cross-correlations in configuration space. We use the estimator of Ref. [60], in which the correlation function is weighted by  $r^{-1}$  to increase the signal-to-noise ratio:

$$\bar{w}_{\text{sp}}(z) = \sum_i r_i^{-1} \Delta r_i w_{\text{sp,binned}}(r_i, z) \quad (5.2)$$

where we use three log-spaced bins in  $r$  between 2.5 and  $10 h^{-1}$  Mpc. The binned correlation function is given by

$$w_{\text{sp,binned}}(r_i, z) = \int \frac{\ell d\ell}{2\pi} C_\ell^{\text{p-s cross}} \frac{1}{\pi(r_{\text{max},i}^2 - r_{\text{min},i}^2)} \int_{r_{\text{min},i}}^{r_{\text{max},i}} 2\pi r dr J_0(\ell\theta) \quad (5.3)$$

Noticing that  $\theta = r/\chi$ <sup>12</sup> and switching integration variables from  $\ell$  to  $k$  we can write

$$\bar{w}_{\text{sp}}(z) = b_{\text{sml},s}(z) b_{\text{sml},p}(z) H(z) \frac{dN_p}{dz} I(z) + \bar{w}_{\text{mag}}(z) \quad (5.4)$$

with

$$I(z) = \int \frac{k dk}{2\pi} \int_{z_{\text{min}}}^{z_{\text{max}}} dz \frac{dN_s}{dz} P_{\text{mm}}(k, z) \sum_{r_i} \frac{r_i^{-1} \Delta r_i}{\pi r_{\text{max},i}^2 - \pi r_{\text{min},i}^2} \int_{r_{\text{min},i}}^{r_{\text{max},i}} 2\pi r J_0(kr) dr \quad (5.5)$$

In the linear regime  $I(z)$  is equal to  $D^2(z)$  times a redshift-independent integral, which is degenerate with the normalization of  $dN_p/dz$ . On our scales of interest,  $I(z)$  deviates only slightly from  $D^2(z)$  ( $\sim 5\%$  at  $z = 2$ ). To compute  $I(z)$  we use the HaloFit nonlinear matter power spectrum from Ref. [75] for  $P_{\text{mm}}(k, z)$  and continue to assume scale-independent bias.

Lensing magnification can correlate samples widely separated in redshift and therefore bias clustering redshifts in the tails of the distribution [59, 73]. We estimate the contribution

<sup>12</sup> When measuring  $w(\theta)$ , we count pairs in angular bins with  $\theta_i = r_i/\chi_{\text{central}}$ , where  $\chi_{\text{central}}$  is the comoving distance to the center of the sub-bin. Therefore, within each sub-bin,  $r = \theta\chi_{\text{central}}$ , which is well approximated by  $r = \theta\chi$  because the sub-bins are narrow. This simplifies the triple integral in Equation 5.5 by allowing the  $r$  integral to be redshift-independent.

of magnification bias  $\bar{w}_{\text{mag}}(z)$  using the COSMOS cross-match  $dN/dz$  and the measured  $s$  for unWISE and the spectroscopic samples (Appendix C), and assuming a scale-independent bias times the HaloFit power spectrum. We use the following form for the bias evolution of each sample:

$$b_{\text{sml,p}}(z) = 0.8 + 1.2z \quad \text{Blue} \quad (5.6a)$$

$$b_{\text{sml,p}}(z) = \max(1.6z^2, 1) \quad \text{Green} \quad (5.6b)$$

$$b_{\text{sml,p}}(z) = \max(2z^{1.5}, 1) \quad \text{Red} \quad (5.6c)$$

which is roughly consistent both with the observed clustering given the cross-match  $dN/dz$  and the expected bias evolution from a simple HOD of the unWISE samples (Figure 16). We show  $\bar{w}$  and the magnification bias correction in Figure 3. Magnification bias has the largest impact on the blue sample, with CMASS galaxies at  $z > 0.6$  showing the largest impacts.

We can invert Equation 5.4 to derive  $b_{\text{p,sml}}dN_{\text{p}}/dz$  given a measurement of  $\bar{w}_{\text{sp}}$ . We measure the binned correlation function using the estimator of ref. [76]

$$\hat{w}_{\text{sp,binned}}(\theta) = \frac{D_{\text{s}}D_{\text{p}}}{D_{\text{s}}R_{\text{p}}} \frac{N_{\text{R}}}{N_{\text{D}}} - 1 \quad (5.7)$$

using three log-spaced bins between<sup>13</sup> 2.5 and 10  $h^{-1}$  Mpc, with the inner radius set to reduce the contributions from scale-dependent bias and “1-halo” effects. Since the unWISE galaxy density varies across the sky (slightly decreasing towards the Galactic center), we set the normalization  $N_{\text{R}}/N_{\text{D}}(\theta)$  by measuring  $N_{\text{R}}/N_{\text{D}}$  in NSIDE = 8 HEALPix pixels and averaging within each annulus about every spectroscopic object.

We cross-correlate the unWISE photometric galaxies with spectroscopic quasars from BOSS DR12 [77] and eBOSS DR14 [78]<sup>14</sup> and galaxies from BOSS CMASS and LOWZ [79]. We plot the redshift and sky distributions of the spectroscopic samples used for the clustering redshifts in Figure 2.

We split the spectroscopic samples into bins of width  $\Delta z = 0.05$  at  $z < 0.8$  and  $\Delta z = 0.2$  at  $z > 0.8$  where the errorbars become much larger due to the sparser quasar samples. As  $\Delta z$  becomes narrower, the signal-to-noise in each individual bin decreases, but the total signal-to-noise of  $dN/dz$  increases modestly (by  $\sim 35\%$  as  $\Delta z$  changes from 0.1 to 0.02). We prefer having a relatively high signal-to-noise in the individual bins, particularly at high redshift where  $dN/dz$  is nearly zero but our errorbars are also relatively large.

We restrict the BOSS quasars to the “CORE”-like sample from ref. [80] (similar to the “QSO\_CORE\_MAIN” targeting flag, but only including quasars that would have been selected by the [81],<sup>15</sup> and removing quasars lying in regions where the targeting completeness is  $< 75\%$ ), as was done in previous quasar clustering analyses [80, 82]. We remove all objects in the southern galactic cap (SGC), which are a small fraction of the total spectroscopic sample. Differences in photometric calibration between the SGC and NGC lead to slightly different galaxy samples [83, 84], unexplained differences in quasar clustering between NGC and SGC [80, 82, 85], and differences in  $\hat{w}_{\text{sp}}$ , possibly resulting from the different spectroscopic bias

<sup>13</sup>At all redshifts, the lower limit corresponds to much larger angular scales than those affected by the WISE PSF and suppression by nearby bright sources; see Fig. 25 in [http://wise2.ipac.caltech.edu/docs/release/allsky/expsup/sec6\\_2.html#brt\\_stars](http://wise2.ipac.caltech.edu/docs/release/allsky/expsup/sec6_2.html#brt_stars) for estimation of this scale.

<sup>14</sup>While the BOSS and SDSS quasar catalogs are independent, eBOSS includes previously observed quasars. We remove these quasars to create an independent sample; they comprise 45% of the northern eBOSS catalog.

<sup>15</sup><https://xdqso.readthedocs.io/en/latest/>

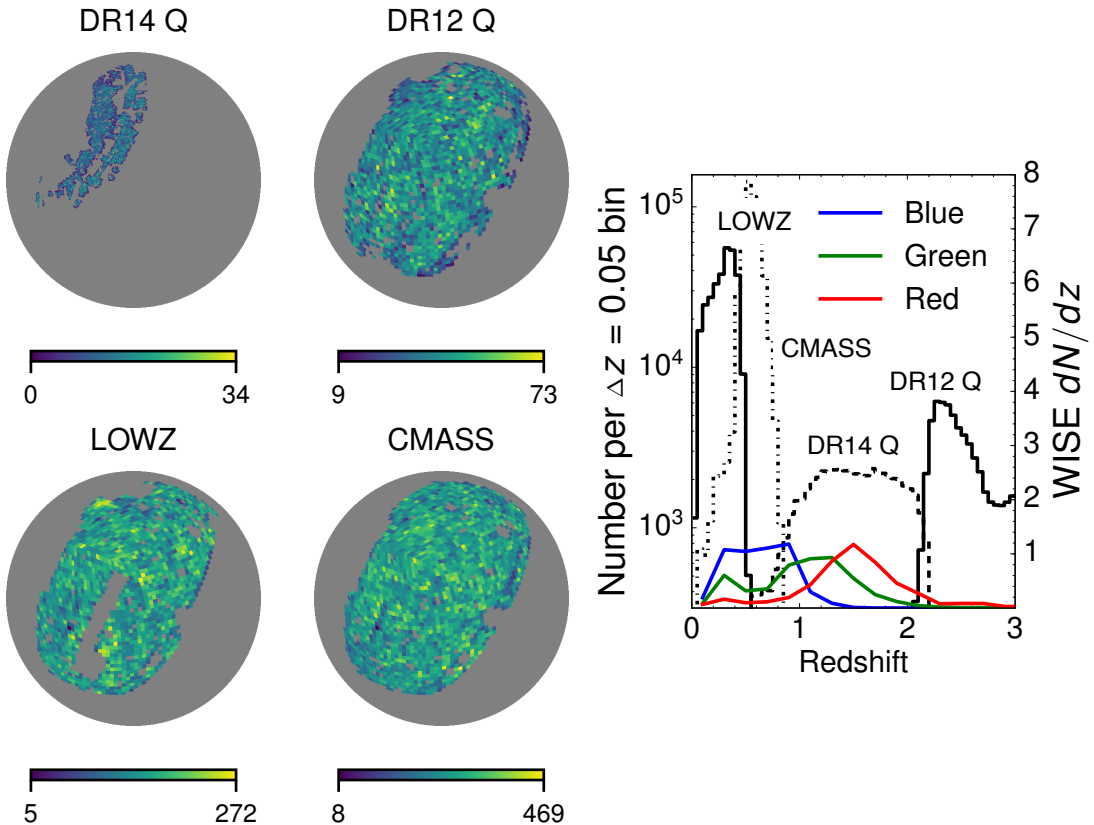


**Figure 2.** *Left:* Sky maps of spectroscopic samples used for cross-correlation redshifts in Galactic coordinates. *Right:* Redshift distributions of spectroscopic samples (black curves) used for cross-correlation redshifts. unWISE galaxy distributions (colored curves) are overplotted with arbitrary amplitude.

evolution. We remove DR12 quasars at  $z < 2$ , DR14 quasars at  $z > 2.2$ , and DR14 quasars at  $z < 0.8$ , since these objects are outliers with redshifts different from each survey’s target redshift range and thus may have different clustering properties than the sample as a whole (indeed, we find somewhat discrepant measurements of  $\bar{w}_{\text{sp}}$  when comparing to BOSS and eBOSS quasars outside their primary redshift ranges). We also remove CMASS galaxies at  $z > 0.8$  and  $z < 0.1$  and LOWZ galaxies at  $z > 0.5$ , where the spectroscopic samples become too sparse to measure  $b_{\text{sm},s}$  (see below). We summarize the key properties of these samples in Table 2.

We apply the corresponding spectroscopic mask to each sample. For eBOSS we use the BOSS veto masks [79], pixelized to  $\text{NSIDE} = 256$  HEALPix pixels, and we also mask  $\text{NSIDE} = 128$  pixels where more than 80% of eBOSS quasars are in DR7 or DR12. For DR12 quasars, we apply the BOSS veto masks [79] and remove  $\text{NSIDE} = 256$  pixels with  $< 75\%$  completeness as computed from the BOSSQSOMASK software<sup>16</sup> [80, 82]. For CMASS and LOWZ we use the corresponding BOSS DR12 LSS catalog masks.<sup>17</sup> We also apply the same WISE masks

<sup>16</sup><http://faraday.uwyo.edu/~admyers/bossqsomask/>

<sup>17</sup><https://data.sdss.org/sas/dr12/boss/lss/>

| Sample | $z_{\min}$ | $z_{\max}$ | $N$    | Jackknife regions | Area (deg <sup>2</sup> ) |
|--------|------------|------------|--------|-------------------|--------------------------|
| DR14 Q | 0.8        | 2.2        | 54708  | 29                | 1178                     |
| DR12 Q | 2.0        | 4.0        | 67175  | 34                | 6030                     |
| LOWZ   | 0.0        | 0.5        | 273549 | 31                | 5656                     |
| CMASS  | 0.1        | 0.8        | 544308 | 37                | 6670                     |

**Table 2.** Properties of the spectroscopic samples used for cross-correlation redshifts.

that we use for the cross-correlation analysis. For the spectroscopic cross-correlations, we threshold all masks by setting pixels with mask value  $< 0.9$  to zero and  $> 0.9$  to one.

We use jackknife<sup>18</sup> resampling to estimate errors on  $\bar{w}_{\text{sp}}$ . We start by splitting the sky into  $\text{NSIDE} = 4$  HEALPix pixels<sup>19</sup> and then combine neighboring pixels until the unmasked area within each region reaches a threshold, which we vary between 80 and 120% of the maximum pixel area, choosing the threshold that minimizes the difference between the largest and smallest regions. We list the number of regions used for each sample in Table 2. The error on  $\bar{w}_{\text{sp}}$  is then

$$\sigma_w^2(z) = \sum_{L=1}^N \frac{R_{[L]}}{R} (\bar{w}_{[L]}(z) - \langle \bar{w}(z) \rangle)^2 \quad (5.8)$$

where  $R$  refers to the number of randoms, the subscript  $[L]$  indicates that we exclude the  $L$ th region, and  $\langle \bar{w}(z) \rangle$  is the average over all  $N$  jackknife resamples  $\bar{w}_{[L]}(z)$ . The replacement of the conventional factor  $(N-1)/N$  with  $R_{[L]}/R$  is an empirical correction for the fact that the regions have different areas [89].

Combining multiple spectroscopic tracers (as is necessary in our case, due to the broad  $dN/dz$  of the unWISE samples) requires a measurement of  $b_{\text{sml},s}(z)$ . We measure  $b_{\text{sml},s}(z)$  by fitting a scale-independent bias times Halofit to the measured  $w(\theta)$  between 2.5 and 10  $h^{-1}$  Mpc:

$$w_{\text{auto},s}(\theta, z) = b_{\text{sml},s}^2(z) \int_0^\infty k dk P_{\text{mm}}(k) \int_{\chi_{\min}}^{\chi_{\max}} \frac{d\chi}{2\pi} J_0(k\chi\theta) \left( \frac{dN_s}{d\chi} \right)^2 \quad (5.9)$$

where the integral over  $\chi$  ranges between the lower and upper boundaries of each redshift bin. We omit SDSS DR7 quasars from our spectroscopic samples due to their poorly measured autocorrelation [90]. For BOSS galaxies and eBOSS quasars we use publicly available galaxy and random catalogs,<sup>20</sup> and for DR12 quasars we generate randoms using BOSSQSOMASK.

<sup>18</sup>We also investigated bootstrap resampling to estimate the covariance matrix of  $w(\theta)$ , and found that on scales smaller than the resampling pixel size (which is always larger than  $\theta_{\max}$ ), jackknife errors agree well with errors from the “marked bootstrap” of Refs. [86, 87]. We prefer jackknife errors to bootstrap errors because sampling a pixel more than once double-counts all pairs in that pixel and is not a reasonable physical situation. Moreover, it leads to ambiguities in the situation where a spectroscopic source lies in pixel  $i$  and a photometric source lies in pixel  $j$ . In a naive implementation of the bootstrap, intra-pixel pairs are resampled 0, 1, 2... $N$  times while cross-pixel pairs are resampled 0, 1, 4... $N \times M$  times, leading to larger variance on all scales than jackknife or marked bootstrap. The marked bootstrap avoids this issue by resampling only one of the tracers. We also find very little difference between leave-one-out jackknife resampling and leave-two-out jackknife, so we opt for leave-one-out jackknife in the interest of simplicity.

<sup>19</sup>We use  $\text{NSIDE} = 8$  pixels for the smaller-area eBOSS samples. We find that using too small pixels can underestimate the errorbars (e.g. Ref. [88]), so we set the size of the resampling pixels so that  $\sim 30$  are available for each sample.

<sup>20</sup><https://data.sdss.org/sas/dr12/booss/lss/> for BOSS and <https://data.sdss.org/sas/dr14/ebooss/lss/> for eBOSS.

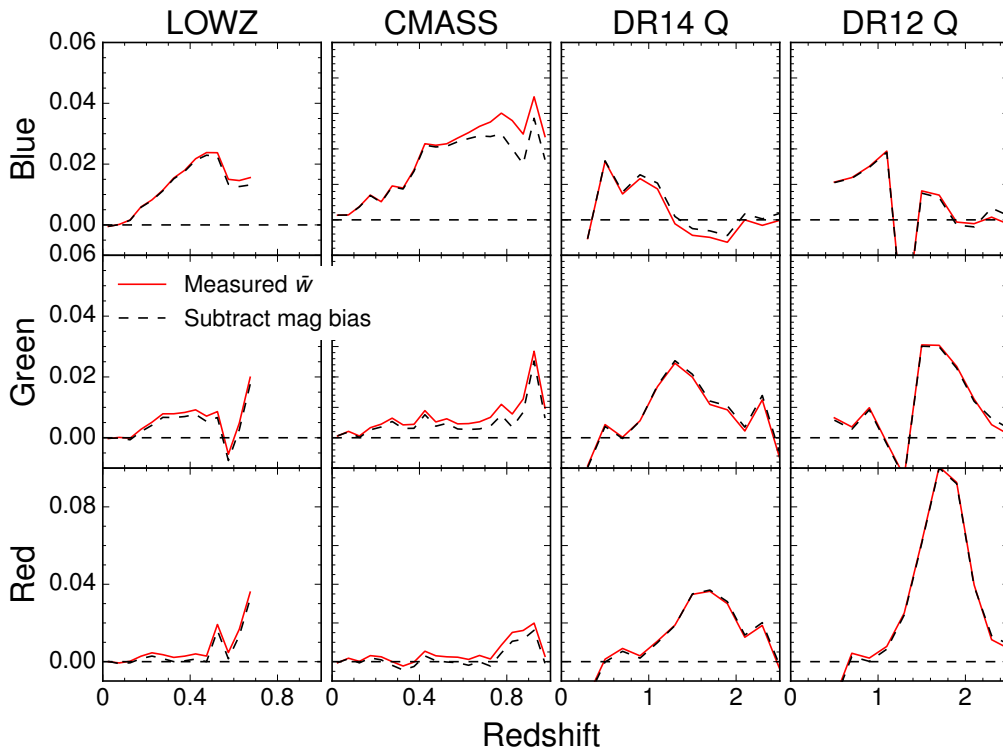


**Figure 3.** Measured  $\bar{w}$  without (black dashed) and with (red solid) magnification bias subtracted for unWISE galaxies crossed with our spectroscopic samples (labeled above each column).

For BOSS galaxies and eBOSS quasars we weight each object by the combined angular systematics, fiber collision and redshift failure weight (Equation 50 in ref. [79]), and for BOSS quasars we weight by the inverse of the targeting completeness [80, 82]. Note that the  $55''$  SDSS fiber collision radius is smaller than our inner bin of  $2.5 h^{-1}\text{Mpc}$  at all redshifts that we consider. While previous measurements of the clustering exist for all spectroscopic samples, we find that the detailed redshift evolution of the BOSS galaxies differs from the assumption of passive bias evolution [91] (obtained from coarse redshift binning) particularly at the low- and high-redshift edges. Therefore in Equation 5.4, rather than rely on previous results, we use the measured  $b_{\text{sml}}(z)$  for LOWZ and CMASS (Figure 4 and Table 7), propagating error from the fitting error on the spectroscopic bias. For quasars, we find that the fitting function of ref. [92] provides a very good approximation to the measured bias evolution:

$$b_{\text{sml},s}(z) = (0.278 \pm 0.018) \left[ (1+z)^2 - 6.565 \right] + (2.393 \pm 0.042) \quad (5.10)$$

We combine the cross-correlation measurements for each of the three spectroscopic samples (quasars, CMASS and LOWZ) by inverse-variance weighting in each redshift bin. We find good agreement between the clustering redshift measurements from CMASS and LOWZ in the redshift range where they overlap ( $0 < z < 0.5$ ) with  $\chi^2 = 12.1$  over 10 dof (7.7/10, 2.8/10) for the blue (green, red) samples.

To model the angular power spectra, the redshift distribution must satisfy physical constraints ( $b_{\text{sml},p} dN_p/dz > 0$  and  $b_{\text{sml},p} dN_p/dz|_{z=0} = 0$ ) and have well-characterized uncer-

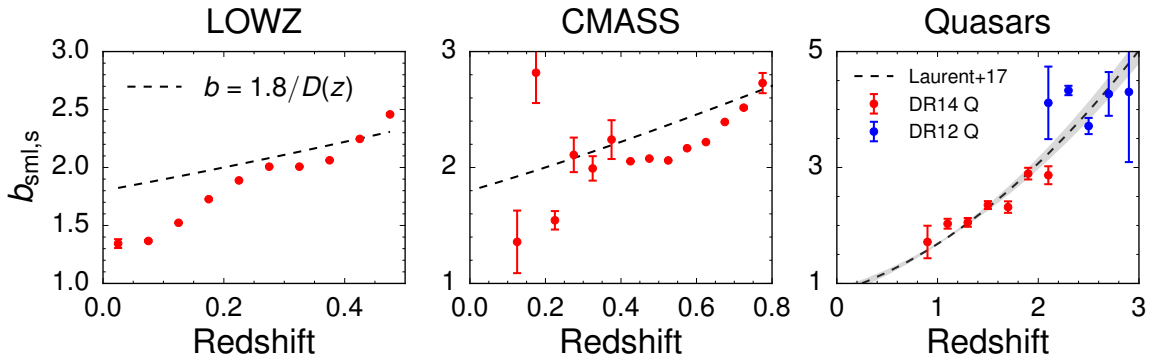


**Figure 4.** Measured bias,  $b_{\text{sml},s}$ , of spectroscopic samples as a function of redshift. The dashed line in the left and center panels shows the ‘passive evolution’ prediction ( $b \propto D^{-1}$ ) while in the right panel it corresponds to the fit from ref. [92] (with the gray band giving uncertainty in the fit). See Table 7 for a tabulated compilation.

tainties. We therefore model  $b_{\text{sml},p}dN_p/dz$  using cubic B-splines with the spline coefficients required to be positive, satisfying the positivity constraint on  $b_{\text{sml},p}dN_p/dz$ . Considering the penalized  $\chi^2$ :

$$\chi^2 = \sum_i \left( \frac{\hat{y}_i - y_i}{\sigma_i} \right)^2 + \lambda \int dx [\hat{y}''(x)]^2 \quad (5.11)$$

we determine  $\lambda$  by minimizing  $\chi^2$  using cross-validation [93]. This method is sufficiently flexible to fit almost any shape of  $b_{\text{sml},p}dN_p/dz$ , while satisfying our constraints. We use knots evenly spaced between  $z = 0.1$  and  $z = 3.5$  with  $\Delta z = 0.2$ .

By requiring  $\hat{y}$  to be positive, this procedure introduces a noise bias into the theory predictions for  $C_\ell$ , since in regions of nearly zero  $dN/dz$ , we will fit to positive noise fluctuations but not negative noise fluctuations. Moreover, the magnitude of this noise bias is different for  $C_\ell^{\kappa g}$  and  $C_\ell^{gg}$ . We find that the differential noise bias is generally small ( $< 5\%$ ) and therefore do not consider it further in this paper. However, cosmological parameter constraints from these data will require a more careful approach [25], such as simulating the  $C_\ell$  and  $dN/dz$  measurement given some known input cosmology and  $dN/dz$ , and subtracting the ‘‘mean-field’’ contribution to  $C_\ell$  from the noise bias in  $dN/dz$ .

We create smooth  $dN/dz$  in a similar fashion for the cross-match redshifts. Here we use bins of  $\Delta z = 0.06$  instead, as we find that more knots are required to accurately represent the shape of the cross-match  $dN/dz$ .

We propagate errors on  $dN/dz$  by drawing 100 samples from the data (assuming uncorrelated Gaussian errors between redshift bins), finding the best-fit  $dN/dz$ , and using it to model the auto and cross-power spectra. Additionally, we test the assumptions behind the jackknife  $dN/dz$  errors by splitting the sky in half at Galactic  $\ell = 155^\circ$  and measuring  $dN/dz$  separately for each half. Summary statistics for both the cross-correlation and cross-match redshifts are given in Table 3.

### 5.3 Systematic errors in the cross-correlation $dN/dz$

One source of systematic error in the measurement of  $dN/dz$  is the discrepancy between  $b_{\text{sml},p}$ , as measured by the configuration space photometric-spectroscopic cross-correlations,

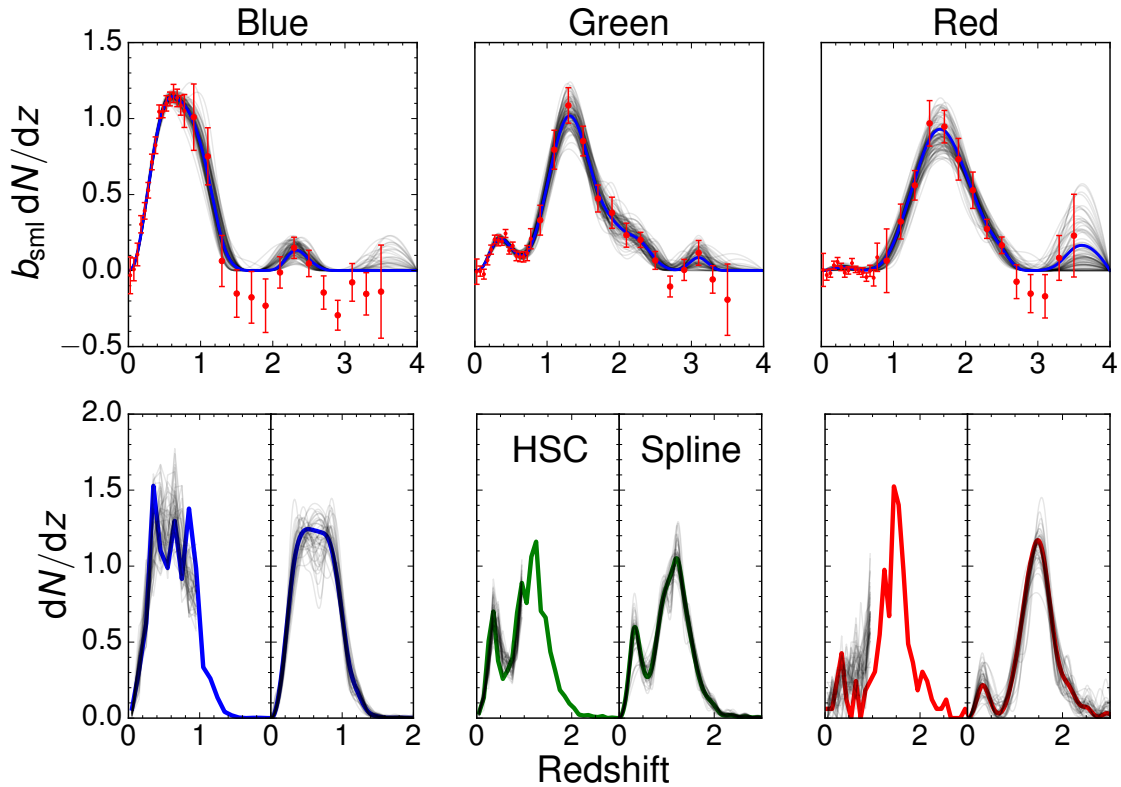


**Figure 5.** *Top:*  $b_{\text{sml,p}}dN_p/dz$  combined for all tracers, with best-fit spline plotted in blue and 100 splined samples drawn from diagonal Gaussian realizations of the noise overplotted in gray. The difference in  $dN/dz$  between the two halves of the sky (split at  $\ell = 155^\circ$ ) is comparable to the range of the 100 spline realizations. *Bottom:*  $dN/dz$  from the COSMOS cross-matches (thick solid lines; measurement in left panels and spline fit in right panels) compared to  $dN/dz$  from 44  $\sim 2\text{deg}^2$  patches of HSC (gray lines, left panels) and 44 splined samples drawn from diagonal Gaussian realizations of the noise (gray lines, right panels). While HSC is deep enough to contain nearly all of the WISE objects, its photometric redshifts become biased at  $z > 1$  and therefore we do not display them beyond  $z = 1$ .

| Color | Median $z$<br>( $b$ -weighted) | Std   | Percentile<br>(5%-95%) | Median $z$<br>$\ell < 155^\circ$ | Median $z$<br>$\ell > 155^\circ$ | Median $z$ | Std   | Percentile<br>(5%-95%) |
|-------|--------------------------------|-------|------------------------|----------------------------------|----------------------------------|------------|-------|------------------------|
| Blue  | 0.72                           | 0.031 | 0.11                   | 0.75                             | 0.72                             | 0.63       | 0.022 | 0.06                   |
| Green | 1.38                           | 0.026 | 0.09                   | 1.35                             | 1.38                             | 1.09       | 0.019 | 0.06                   |
| Red   | 1.70                           | 0.064 | 0.23                   | 1.71                             | 1.68                             | 1.46       | 0.030 | 0.09                   |

**Table 3.** Summary statistics of the redshift distribution of the WISE sample. Statistics on the left are computed from samples of  $b_{\text{sml,p}}dN_p/dz$  (i.e. clustering redshifts), while statistics on the right are computed from samples of the cross-match  $dN/dz$ . Std gives the standard deviation of the medians of the 100  $dN/dz$  samples.

and  $b_{\text{lin,p}}$ , as required to model the autospectra and CMB cross-spectra. Exactly matching the scales used for the cross-correlation redshifts and the CMB cross-correlations is undesirable because it would push the cross-correlation redshifts to large scales where the signal-to-noise is lower and the potential impact of observational systematics is larger [60]; indeed, previous

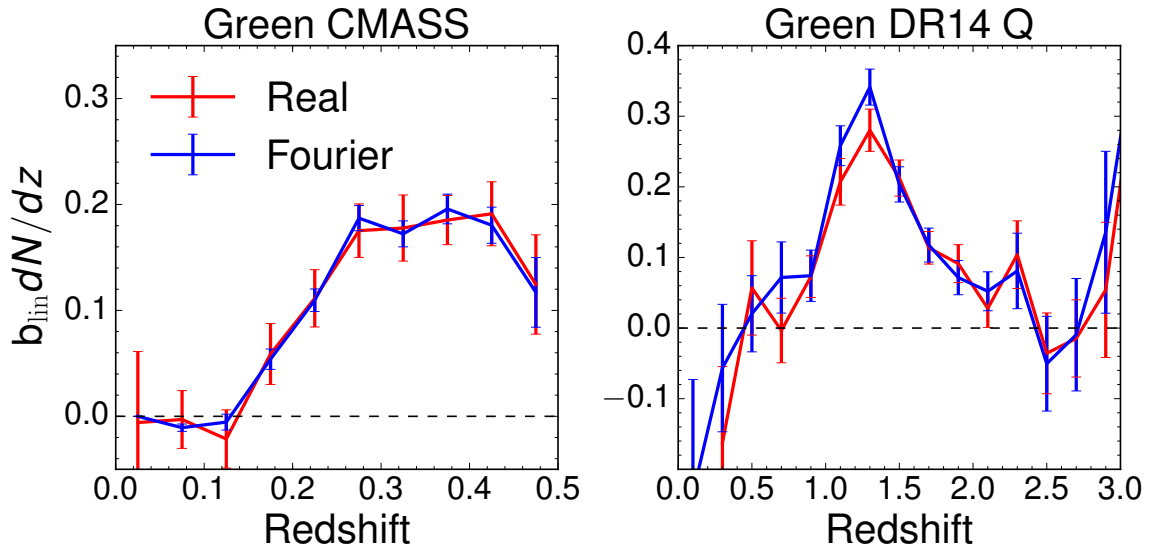


**Figure 6.** Comparison between the fiducial  $b_{\text{sml,p}}dN_{\text{p}}/dz$  measured in configuration space (Equation 5.4) and  $b_{\text{lin,p}}dN_{\text{p}}/dz$  measured in harmonic space using the pipeline described in Section 4, with  $300 < \ell < 1000$ .

work uses scales of several Mpc at most [60, 63, 65–67, 71–73]. Conversely working on very small scales can be problematic, as the cross-correlation could depend upon galaxy formation physics in addition to the redshift distribution.

To study potential deviations between  $b_{\text{sml,p}}$  and  $b_{\text{lin,p}}$ , we populate an  $N$ -body simulation with a simple HOD model for the WISE galaxies (Appendix B), which is roughly consistent with the spectroscopic cross-clustering given the cross-match  $dN/dz$  (Figure 16). We then measure  $b_{\text{sml}}$  and  $b_{\text{lin}}$  from the autocorrelation of halos in the simulation at four representative redshifts ( $z = 0.41, 1.00, 1.27$  and  $1.78$ ; Figure 14). At  $z = 0.41$ ,  $b_{\text{sml}}$  is 0.7% (1.7%, 2.5%) greater than  $b_{\text{lin}}$  for halos representative of the blue (green, red) samples. At  $z = 1.78$ ,  $b_{\text{sml}}$  is 7.2% (15.3%) greater than  $b_{\text{lin}}$  for green (red) halos; and at  $z = 1.00$ ,  $b_{\text{sml}}$  is 1.6% greater than  $b_{\text{lin}}$  for blue halos. We discuss the implications of these discrepancies between  $b_{\text{sml,p}}$  and  $b_{\text{lin,p}}$  in Section 7; we find that their impact is subdominant to the statistical uncertainty on  $dN/dz$ .

We also compare the fiducial real-space  $b_{\text{sml,p}}dN_{\text{p}}/dz$  to  $b_{\text{lin,p}}dN_{\text{p}}/dz$  measured in Fourier space using Eq. 5.1 on the same angular scales ( $\ell = 300$  to 1000) as the CMB lensing cross-correlation.<sup>21</sup> We find good agreement for  $bdN/dz$  in both configuration and harmonic space (Figure 6), suggesting that discrepancies between  $b_{\text{sml,p}}dN_{\text{p}}/dz$  and  $b_{\text{lin,p}}dN_{\text{p}}/dz$  are minor.

We test the sensitivity of the  $dN/dz$  results to the presence of angular systematics in the spectroscopic data by measuring the weighted cross-correlation, using the combined angular systematics, fiber collision and redshift failure weights for BOSS galaxies and eBOSS; and the inverse of the targeting completeness for BOSS quasars. We found  $< 0.5\sigma$  change between the weighted and unweighted cross-correlations among all bins in redshift, spectroscopic and photometric tracers; this suggests that angular systematics correlated with unWISE fluctuations

<sup>21</sup>At  $z < 0.3$ ,  $\ell_{\text{max}} = 1000$  corresponds to  $k_{\text{max}} > 1 h \text{ Mpc}^{-1}$ , and the scale-independent bias assumption begins to break down. As a result, we set  $\ell_{\text{max}} = \min(1000, k_{\text{max}}\chi)$ , where  $\chi$  is the comoving distance to the redshift bin center and  $k_{\text{max}} = 2.5 h \text{ Mpc}^{-1}$ .

negligibly affect our results.

We also compare the observed cross-correlation in a given redshift bin to the cross-correlation between Gaia stars and the spectroscopic sample. Since  $\sim 2\%$  of all unWISE samples are stars, star-driven fluctuations in the spectroscopic sample may lead to spurious correlations between unWISE and spectroscopic samples. We find that the LOWZ-Gaia cross-correlation, times a fiducial stellar contamination fraction of 2%, is  $< 5\%$  of the LOWZ-unWISE cross-correlation at  $z > 0.15$ , but comparable to the LOWZ-unWISE cross-correlation at  $z < 0.15$  (for all three colors), although the error bars on the LOWZ-Gaia cross-correlation are comparable to the measured cross-correlation at these redshifts.

## 6 Galaxy-lensing auto and cross-spectra

In this section we present our measurements. We parameterize the amplitude of the correlations by a single effective linear bias

$$b^{\text{eff}} = \int dz b_{\text{lin,p}}(z) \frac{dN_{\text{p}}}{dz} \quad (6.1)$$

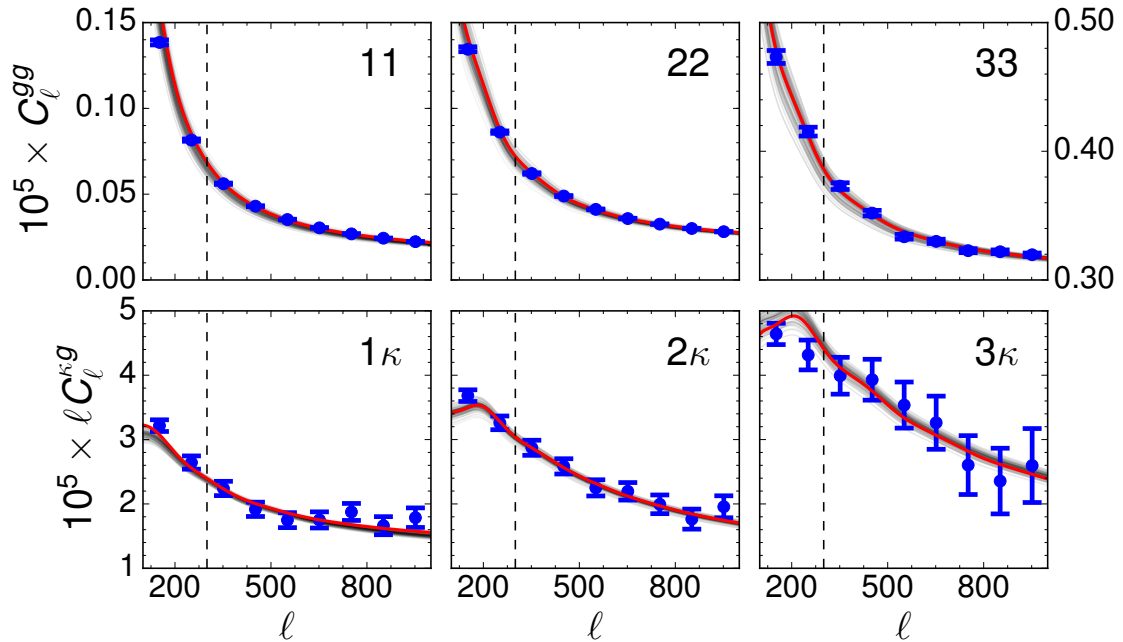
where we follow our convention of  $\int dz dN/dz = 1$ . For our theory model, we take the cross-correlation redshifts as our fiducial redshift distribution, while for the magnification bias term, we take the cross-matched  $dN/dz$ , and the values of  $s$  from Appendix C. This is because the cross-correlation redshifts measure the product of the photometric sample bias (including its redshift evolution) and the redshift distribution,  $b_{\text{phot}}(z) \times (dN/dz)_{\text{phot}}$  if we assume that the bias and redshifts of the spectroscopic sample are known. On the other hand, the cross-matched redshifts with COSMOS measure  $(dN/dz)_{\text{phot}}$  directly without any dependence on the bias.

Figure 7 shows the auto correlation of our three galaxy samples as well as their cross-correlation with the CMB lensing convergence,  $\kappa$ . Table 4 summarizes the results. We quote both statistical and  $dN/dz$  error bars on  $b^{\text{eff}}$ ; the statistical errors are from the errors on  $C_{\ell}^{gg}$  and  $C_{\ell}^{\kappa g}$  using the fiducial  $dN/dz$ , whereas the  $dN/dz$  error bars are the standard deviation of  $b^{\text{eff}}$  from fitting  $C_{\ell}^{gg}$  and  $C_{\ell}^{\kappa g}$  to 100 samples of  $dN/dz$  with uncorrelated Gaussian error added (as described earlier).

Over the range of scales that we model ( $300 < \ell < 1000$ ), we obtain cross-correlation  $S/N = \sqrt{\chi_{\text{null}}^2 - \chi_{\text{cross}}^2}$  of 40.0, 45.8 and 24.1 for the blue, green and red samples, respectively. The combined cross-correlation  $S/N$  for the sample as a whole (taking into account the covariance between the three galaxy samples) is 58.7.

| WISE sample | $b_{\text{auto}}^{\text{eff}}$ | Shot Noise ( $\times 10^7$ ) | $\sigma_b$ from $dN/dz$ | $\chi_{\text{auto}}^2/\text{dof}$ | $b_{\text{cross}}^{\text{eff}}$ | $\sigma_b$ from $dN/dz$ | $\chi_{\text{cross}}^2/\text{dof}$ |
|-------------|--------------------------------|------------------------------|-------------------------|-----------------------------------|---------------------------------|-------------------------|------------------------------------|
| Blue        | $1.71 \pm 0.0072$              | $0.97 \pm 0.015$             | 0.0842                  | 16.7/4                            | $1.56 \pm 0.0393$               | 0.0329                  | 6.04/5                             |
| Green       | $2.46 \pm 0.0121$              | $1.87 \pm 0.015$             | 0.0788                  | 4.16/4                            | $2.25 \pm 0.0520$               | 0.0271                  | 2.44/5                             |
| Red         | $3.29 \pm 0.0787$              | $30.4 \pm 0.13$              | 0.267                   | 9.82/4                            | $3.49 \pm 0.161$                | 0.1371                  | 1.66/5                             |

**Table 4.** Results from fitting a constant bias times HaloFit power spectrum (using cross-correlation  $dN/dz$ ). Note that the value of  $\chi^2$  here is for a *fixed* fiducial  $dN/dz$  and for a linear bias model with HaloFit power spectrum. A high  $\chi^2$  value indicates the need to marginalize over the redshift distribution for any cosmological interpretation, and highlights the importance of going beyond linear bias. In the follow up paper [25], we fully marginalize over the uncertainty in  $dN/dz$  and a non-linear model for galaxy biasing, obtaining a good fit.



**Figure 7.** Auto correlation (top) and cross correlation between the unWISE catalog and Planck CMB lensing (bottom). The best-fit theory curve assuming a constant bias times HaloFit is shown as a solid red line and the uncertainty in the model from the uncertainty in  $dN/dz$  is given by the gray lines. We fit angular scales to the right of the dashed line. Magnification bias is a few times larger than the errorbars in the auto-spectra, and  $\sim 50\%$  of the errorbars in the CMB cross-spectra.

## 7 Systematics in the cross-correlation and null tests

In this section we explore the impact of stellar contamination, foregrounds in the CMB maps and the galactic latitude dependence of the signal.

### 7.1 Stellar Contamination

Due to the photometric nature of the catalog, with only two broad-band filters available, some fraction of the objects in our catalog will be stars or other non-cosmological sources such as nebulae or artifacts in the images. For simplicity, below we shall refer to any non-cosmological source that is uncorrelated with the true galaxies in our samples as “stars.” On scales where stars can be considered unclustered, i.e. where their clustering power is negligible compared to the galaxies, their effect is to lower both the auto and cross correlations in a way that is completely degenerate with the galaxy bias, and hence can be marginalized over in a cosmological analysis. To see this, let’s assume that average number density of objects in our catalog,  $\bar{n}$ , is the sum of galaxies,  $\bar{n}_g$ , and “stars”,  $\bar{n}_s$ . The observed “galaxy overdensity” necessarily includes both

$$g^{\text{obs}} = \frac{\delta n_g}{\bar{n}_g + \bar{n}_s} + \frac{\delta n_s}{\bar{n}_g + \bar{n}_s} \quad (7.1)$$

We expect the second term to be uncorrelated with CMB lensing, given its non-cosmological origin. This is an important assumption that can be violated, for example, if galactic dust emission affects CMB lensing reconstruction, and at the same time modulates the number

density of galaxies observed in WISE. We test this in the next section by applying different galactic cuts. Assuming the second term is uncorrelated with  $\kappa$ , we can write

$$\langle \kappa g^{\text{obs}} \rangle = \langle \kappa g^{\text{true}} \rangle \frac{\bar{n}_g}{\bar{n}_g + \bar{n}_s} = \langle \kappa g^{\text{true}} \rangle \frac{1}{1 + \epsilon_s} \quad (7.2)$$

where we have defined  $\epsilon_s = \bar{n}_s/\bar{n}_g$  to be the stellar contamination fraction. Similarly, on scales where stars are approximately unclustered (see below),

$$\langle g^{\text{obs}} g^{\text{obs}} \rangle = \langle g^{\text{true}} g^{\text{true}} \rangle \left( \frac{1}{1 + \epsilon_s} \right)^2 \quad (7.3)$$

From the argument above, we can see that the effect of stellar contamination is to lower the auto and cross correlations in a scale-independent way. Since  $\langle \kappa g^{\text{true}} \rangle \propto b_g$  and  $\langle g^{\text{true}} g^{\text{true}} \rangle \propto b_g^2$ , we conclude that unclustered stellar contamination is completely degenerate with a scale-independent galaxy bias and that our analysis actually measures the “effective bias”

$$b^{\text{eff}} = b^{\text{true}} \frac{1}{1 + \epsilon_s} \quad (7.4)$$

so that marginalization over galaxy bias will automatically also marginalize over the (in general unknown) amount of stellar contamination. We further note that the ratio

$$\frac{(C_\ell^{\kappa g})^2}{C_\ell^{gg}} \sim \frac{(b_g^{\text{eff}})^2 \sigma_8^4}{(b_g^{\text{eff}})^2 \sigma_8^2} \sim \sigma_8^2 \quad (7.5)$$

is proportional to  $\sigma_8^2$  in linear theory, and is therefore independent of  $b^{\text{eff}}$  on linear scales.

The power spectrum of galactic contaminants such as stars is typically very large on large scales, falling off steeply with increasing  $\ell$  (faster than the typical galaxy power spectrum). For example, we have checked that if the stellar contamination in unWISE traces a Gaia stellar map<sup>22</sup> with stellar contamination fraction  $\sim 1\%$  (as expected from the cross-match to COSMOS), the stellar power in the lowest- $\ell$  bin used in the analysis is  $< 0.5\%$  of the galaxy clustering power on the same scale, ensuring that the argument above holds.

## 7.2 Foreground contamination to CMB lensing cross-correlations

The Minimum Variance (MV) reconstruction we use in the fiducial analysis is dominated by CMB temperature (rather than polarization), and is therefore subject to possible contamination by both galactic and extragalactic foregrounds. When these foregrounds are correlated with the galaxy sample of interest, they can lead to biases in the cross-correlation [29–32, 94].

Regarding galactic foregrounds, we expect the largest contaminant to be galactic dust, seen in emission in the CMB maps, and causing reddening and/or extinction on most galaxy catalogs. Imperfect foreground separation can impact the CMB lensing maps. While we expect the IR-selected unWISE sources not to be directly affected by galactic dust, nonetheless their local density can be dependent on (for example) stellar density, which is itself correlated with galactic dust. The Planck team [24] performed a large number of null tests regarding the reconstructed map, and find general stability of the baseline reconstruction on the SMICA component separated temperature map. Importantly, the reconstruction is stable with respect to choice of galactic mask, with variations consistent with those expected from the change in

<sup>22</sup>We also find a similar power spectrum for Gaia stars that meet our blue or green WISE color selection.

area. Most of the null test tensions come from the reconstruction on the 217 GHz frequency map, which may contain non-negligible galactic contamination. We caution that the tSZ-free map has larger weight given to the 217 GHz channel and may therefore have a larger dust contamination.

Regarding extragalactic foregrounds, semi-analytical models predict that the impact of extragalactic foregrounds should be minimal compared to the Planck lensing error bars, both in auto and cross-correlation [31, 32, 94]. This was tested with realistic correlated CMB and large-scale structure simulations by the Planck team, showing that the maximum bias for the cross-correlation is expected to be around 0.2% [24], considerably below our noise level. As a further test, we repeat the cross-correlation with the Planck 2018 lensing reconstructed from tSZ-deprojected temperature maps, shown in Table 5. Apart from removing the possible tSZ contamination, the CIB contribution will be significantly different due to the different weighting of the single-frequency channels. The consistency between the fiducial and tSZ-free cross-correlations provides further confidence that foreground contamination is subdominant to our other sources of uncertainty.

| WISE sample | $b_{\text{cross}}^{\text{eff}}$ | $\chi_{\text{cross}}^2/\text{dof}$ | $b_{\text{cross,tSZ-free}}^{\text{eff}}$ | $\chi_{\text{cross,tSZ-free}}^2/\text{dof}$ |
|-------------|---------------------------------|------------------------------------|--|---|
| Blue        | $1.56 \pm 0.0393$               | 3.59/4                             | $1.52 \pm 0.0417$                        | 7.20/5                                      |
| Green       | $2.25 \pm 0.0520$               | 2.77/4                             | $2.23 \pm 0.0554$                        | 3.31/5                                      |
| Red 16.2    | $3.49 \pm 0.161$                | 5.11/4                             | $3.43 \pm 0.172$                         | 4.28/5                                      |

**Table 5.** Comparison between fiducial  $b_{\text{cross}}^{\text{eff}}$  (reproducing Table 4) and  $b_{\text{cross,tSZ-free}}^{\text{eff}}$  for the tSZ free sample.

### 7.3 Galactic mask dependence of the sample properties

If the redshift distribution varies across the sky, the clustering  $dN/dz$  measured in the SDSS region could be unrepresentative of the true  $dN/dz$  across the entire WISE mask. We test this possibility by restricting the  $C_{\ell}^{gg}$  and  $C_{\ell}^{\kappa g}$  measurement to the SDSS footprint used to measure  $dN/dz$  and repeating our measurements. We find good agreement between the biases measured in the SDSS region and the biases measured across the full sky (Table 6). We also find that the galaxy-galaxy cross-spectra (i.e. Fig. 19) are quite similar in the SDSS region as in the full unWISE footprint, changing by  $< 10\%$ .

| WISE sample | $b_{\text{auto}}^{\text{eff}}$ | $10^7 \times \text{Shot Noise}$ | $\chi_{\text{auto}}^2/\text{dof}$ | $b_{\text{cross}}^{\text{eff}}$ | $\chi_{\text{cross}}^2/\text{dof}$ |
|-------------|--------------------------------|---------------------------------|-----------------------------------|---------------------------------|------------------------------------|
| Blue        | $1.75 \pm 0.0137$              | $0.90 \pm 0.030$                | 9.80/4                            | $1.61 \pm 0.0772$               | 4.74/5                             |
| Green       | $2.52 \pm 0.0235$              | $1.87 \pm 0.030$                | 0.26/4                            | $2.21 \pm 0.103$                | 3.34/5                             |
| Red 16.2    | $3.28 \pm 0.152$               | $30.4 \pm 0.26$                 | 2.88/4                            | $3.33 \pm 0.314$                | 7.69/5                             |

**Table 6.** Results from fitting a constant bias times HaloFit power spectrum (using cross-correlation  $dN/dz$ ), restricting measurements to the CMASS area.

We further test the impact of restricting our sample to higher Galactic latitudes by sequentially applying the Planck 60%, 40% and 20% Galactic masks (retaining the “cleanest” 60, 40 and 20% of the extragalactic sky)<sup>23</sup> in addition to the standard WISE masks described in Section 2.4. We find no significant change in  $C_{\ell}^{\kappa g}$  as the Galactic masking is changed. In

<sup>23</sup>Available at [https://irsa.ipac.caltech.edu/data/Planck/release\\_2/ancillary-data/masks/HFI\\_Mask\\_GalPlane-apo0\\_2048\\_R2.00.fits](https://irsa.ipac.caltech.edu/data/Planck/release_2/ancillary-data/masks/HFI_Mask_GalPlane-apo0_2048_R2.00.fits)

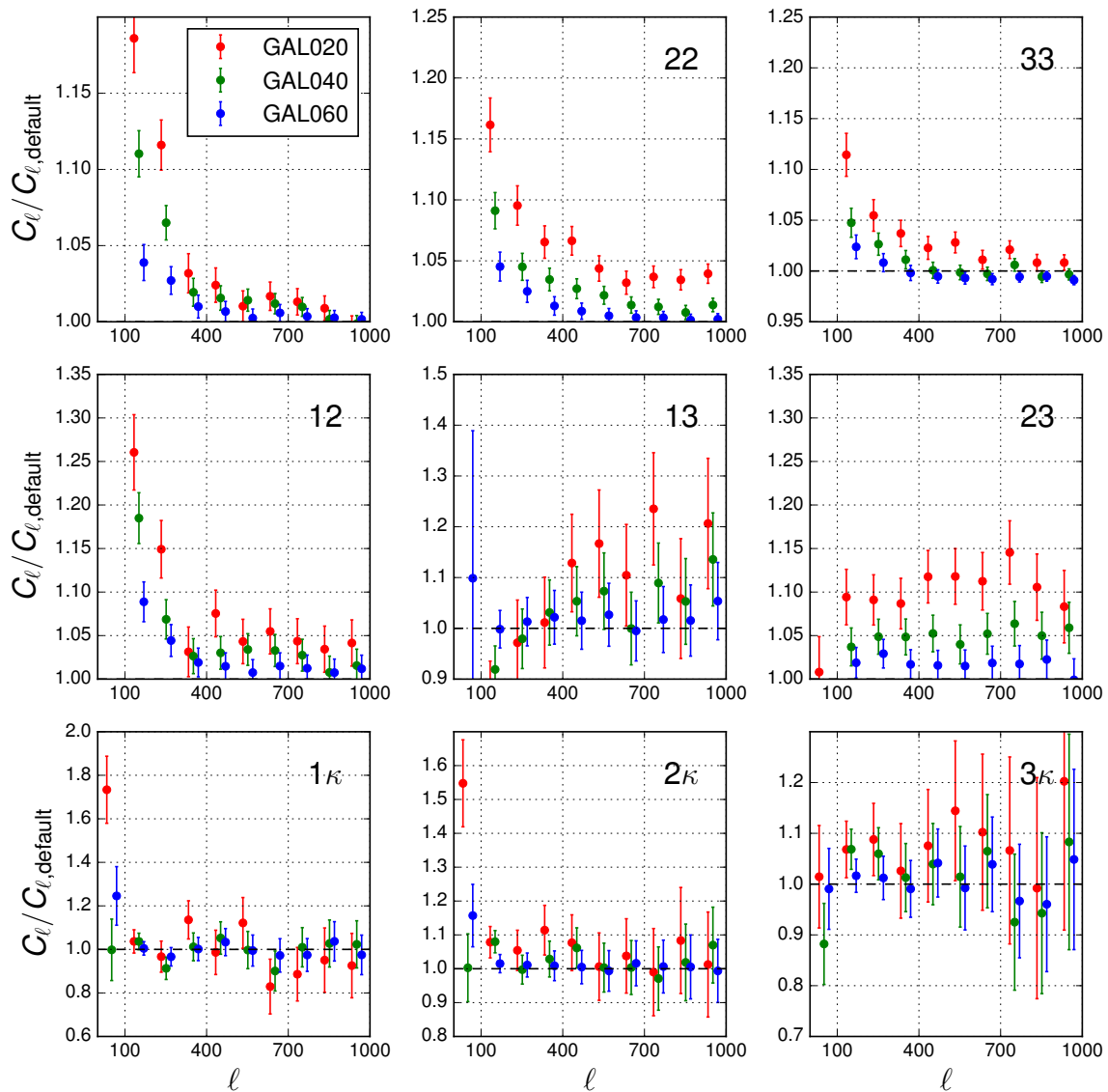


**Figure 8.** Change in clustering when masking is changed from the default Planck and WISE masks to the Planck 20%, 40% and 60% Galactic masks. Top row shows galaxy auto-spectra, middle row shows galaxy-galaxy cross-spectra, and bottom row gives galaxy-CMB cross spectra.

contrast, we find a roughly scale-independent shift of a few percent in  $C_\ell^{gg}$  at  $\ell > 300$ , and a change in shape in  $C_\ell^{gg}$  at  $\ell < 300$ . At  $100 < \ell < 300$ , we find an increase in power at higher Galactic latitudes, whereas at  $\ell < 100$ , we find decreasing power at higher Galactic latitudes. Due to the change in shape of  $C_\ell^{gg}$  at  $\ell < 300$ , which hints at unknown large-scale systematics, we do not fit these scales.

At  $\ell > 300$ , we find a mild scale-independent trend in the amplitude of  $C_\ell^{gg}$  with Galactic latitude, which may be caused by changes in the galaxy population due to changing selection function at higher Galactic latitudes (modifying both the bias and  $dN/dz$ ). This should not affect our cosmological constraints as long as the area over which we measure  $dN/dz$  and the auto and cross correlations are the same. In practice, we prefer not to restrict the

$dN/dz$  measurement to the footprint of the spectroscopic samples ( $f_{\text{sky}} = 0.15$ ) and find that measuring  $b^{\text{eff}}$  over the spectroscopic footprint leads to variations  $< 1\sigma$ , suggesting  $dN/dz$  varying on the sky is not a major systematic.

Changes in the galaxy-galaxy cross-spectra with Galactic latitude suggest that  $dN/dz$  does vary on the sky in addition to the bias. If only the bias were changing as we changed the Galactic masks, the increase in the cross-spectrum would go as the geometric mean of the increase in the individual galaxy auto-spectra, but the red-blue and red-green cross-correlations increase by  $\sim 5-10\%$  more than the geometric mean, implying a varying  $dN/dz$ <sup>24</sup> or more complex bias.

We perform a similar test for masking the ecliptic plane below  $\beta = 30^\circ, 45^\circ, 60^\circ$  and  $80^\circ$ , finding similar scale-dependent trends at  $\ell < 300$ , but with milder deviations from unity in all cases (1 – 3% for the galaxy auto spectra and 5% for the galaxy-galaxy cross spectra). We also find that doubling the WISE stellar masking radius changes  $b^{\text{eff}}$  by less than  $1\sigma$ .

#### 7.4 Systematic uncertainties in the redshift distribution

Due to the  $6''$  WISE PSF, blending is a source of systematic error in the cross-match redshifts, as it could lead to spurious matches with COSMOS. Many of our sources are blended, and it is possible that the low-redshift tails in the red and green samples result from source blending rather than from the presence of low-redshift sources. However, because we only use the cross-match redshifts in the magnification bias term, we expect blending to have a negligible impact on  $b_{\text{auto}}^{\text{eff}}$  and  $b_{\text{cross}}^{\text{eff}}$ . If we replace all unWISE magnitudes in the cross-match with Spitzer 3.6 and  $4.5\ \mu\text{m}$  magnitudes (reducing the possibility of source confusion due to the  $2''$  resolution of Spitzer) and replace the cross-match  $dN/dz$  with the Spitzer  $dN/dz$ , we find shifts of  $< 0.3\sigma$  in the fitted biases.

We study the impact of a discrepancy between  $b_{\text{sml,p}}$  and  $b_{\text{lin,p}}$  using  $b_{\text{sml}}$  and  $b_{\text{lin}}$  from the autocorrelation of WISE-like samples in an  $N$ -body simulation (Appendix B). We parameterize  $b_{\text{sml}}/b_{\text{lin}} = 1 + Az^2$  (smooth curves in Figure 15), allowing  $A$  to vary between zero and twice its fiducial value,  $A_{\text{fid}}$ . For each value of  $A$ , we divide  $b_{\text{sml}} dN/dz$  by  $b_{\text{sml}}/b_{\text{lin}}$  and re-fit  $b_{\text{auto}}^{\text{eff}}$  and  $b_{\text{cross}}^{\text{eff}}$ . We define the uncertainty in  $b^{\text{eff}}$  due to nonlinear bias evolution as half the range between  $b^{\text{eff}}(A = 0)$  and  $b^{\text{eff}}(A = 2A_{\text{fid}})$ . For all three unWISE samples, both the bias and uncertainty in  $b^{\text{eff}}$  from nonlinear bias evolution are  $< 50\%$  the uncertainty in  $b^{\text{eff}}$  from statistical error in  $dN/dz$ .

We summarize the impact of different systematics on  $b_{\text{auto}}^{\text{eff}}$  and  $b_{\text{cross}}^{\text{eff}}$  for the green sample in Figure 9. The analogous plots for the blue and red samples look similar; in fact, green is the only sample to have  $> 1\sigma$  discrepancies from the fiducial value (measured using the quadrature sum of the  $dN/dz$  error and the statistical error), with a  $1.15\sigma$  discrepancy from the  $\ell < 155^\circ$  subsample and a  $1.5\sigma$  discrepancy when the cross-match  $dN/dz$  uses  $s_{\text{min}} = 4\ h^{-1}\ \text{Mpc}$ . For the  $s_{\text{min}} = 4\ h^{-1}\ \text{Mpc}$   $dN/dz$ , we use the error for the  $s_{\text{min}} = 4\ h^{-1}\ \text{Mpc}$   $dN/dz$  for  $\sigma$  rather than the quadrature sum of this error and the error from the fiducial  $s_{\text{min}} = 2.5\ h^{-1}\ \text{Mpc}$   $dN/dz$ , because the two  $dN/dz$  errors are highly correlated.

<sup>24</sup>Using fainter red samples (e.g. with a faint cut at  $W2 = 16.5$  or  $16.7$ ) leads to even larger variation in red cross blue compared to red and blue separately, suggesting that  $dN/dz$  variations are more severe for the fainter red samples.

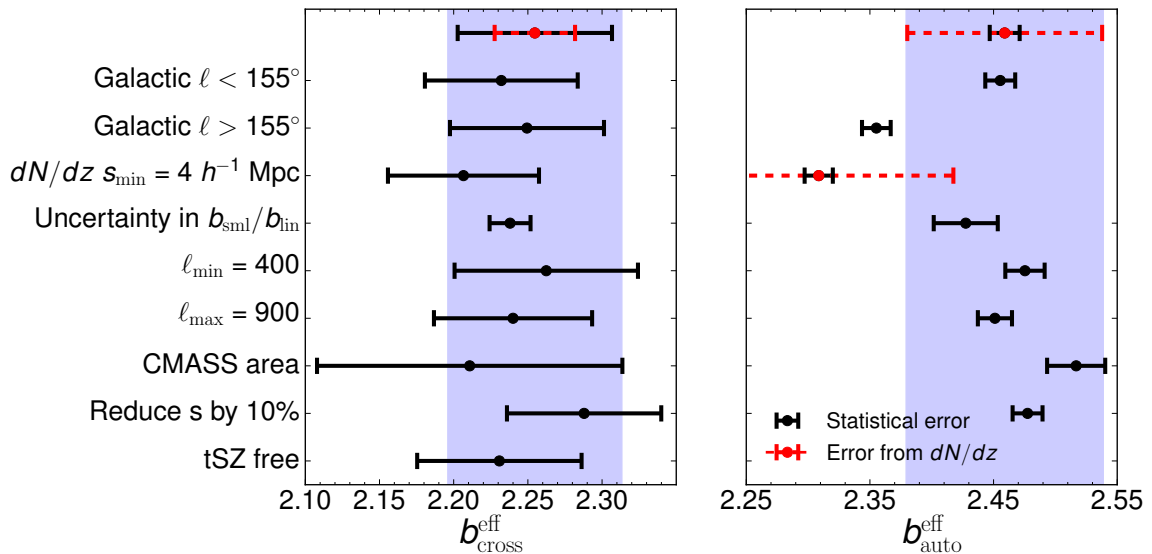


**Figure 9.** Impact of systematic errors on  $b^{\text{eff}}$  for the green sample. Black errorbars give the statistical uncertainty, red dashed errorbars give the systematic uncertainty from errors in  $dN/dz$  (only plotted for the fiducial values), and the blue band displays their quadrature sum. We also plot the uncertainty from  $dN/dz$  error for the  $s_{\text{min}} = 4 h^{-1}$  Mpc  $dN/dz$ , to emphasize that this point is only  $1.5\sigma$  discrepant if we define  $\sigma$  using the fiducial value matching Table 4. The next two rows show  $b^{\text{eff}}$  for the split-sky sample, giving an estimate of uncertainty due to uncertain  $dN/dz$ . The next two rows are concerned with nonlinear bias evolution; either by increasing  $s_{\text{min}}$  to be more robust against nonlinear bias; or using the prescription from Appendix B to estimate the impact and uncertainty of the discrepancy between  $b_{\text{sml,p}}$  and  $b_{\text{lin,p}}$ . The final five rows show the impact of changing scale cuts for the auto- and CMB-cross power spectra, restricting to the CMASS footprint (Table 6), reducing magnification bias response  $s$  by 10%, and using the tSZ-free lensing map (Table 5).

## 8 Conclusions and lessons learned

We have presented a tomographic measurement of the cross-correlation of the unWISE galaxies and CMB lensing. We report a combined detection significance of 58.7, which is the highest-significance detection of lensing by large-scale structure to date.

One of the greatest challenges was the characterization of the redshift distribution for the three samples. Since for most galaxies only the W1 and W2 magnitudes were available, we did not attempt to assign individual photometric redshifts, but just split the full catalog into three samples with different mean redshifts, but with non-negligible overlap between them. We use two techniques to measure the redshift distribution.

First, we cross-match our objects with the COSMOS catalog, obtaining a direct measurement of the redshift distribution  $dN/dz$ . A direct cross-match is insensitive to modeling assumptions and measures  $dN/dz$ , required to calculate the magnification bias contribution. If used to predict clustering, assumptions on the redshift evolution of the bias evolution are necessary. One disadvantage is the high completeness required of the survey, which limits the area available. Another disadvantage is source blending, which could lead to spurious cross-matches and thus modify  $dN/dz$ . The small overlap area (2 square degrees) not only limits the measurement statistically, but given the inhomogeneous depth of the WISE survey and

possible spatial dependence of the selection function, the results may not be representative of the full WISE footprint. While we take steps to ensure that our catalogs are magnitude limited over the whole footprint by applying appropriate magnitude cuts, residual effects such as blending and background subtraction can potentially lead to inhomogeneity in the selection function. The mild trends in bias with respect to Galactic mask observed in Figure 8 may be an indication of this.

Second, we cross-correlate the unWISE samples with a number of overlapping spectroscopic samples, thus determining the product of the bias and redshift distribution. This can be advantageous when calculating the clustering signal, since it is this product that enters the auto-correlation and the cross-correlation with CMB lensing. Another advantage is the typically large overlap area (important for when the selection function is inhomogeneous), and the fact that there are no completeness requirements on the spectroscopic sample. However, assumptions on the redshift evolution of the bias are necessary when calculating the magnification bias contribution, and the impact of magnification needs to be taken into account in the spectroscopic-photometric cross-correlation. Moreover, this measurement is subject to the usual modeling challenges such as non-linearities in clustering and bias.

As discussed in Appendix B, the two measurements of  $dN/dz$  are consistent with each other when assuming a simple model for bias evolution. Further, the consistency of the unWISE bias measured on the CMASS overlap region (Table 6) compared to the whole unWISE footprint (Table 4) indicates that the cross-correlation redshifts should be unaffected by spatial variations in the selection function. In the fiducial analysis, we use the cross-correlation result to predict the clustering and the cross-matched distribution to predict magnification bias and therefore we don't need to assume a redshift evolution of the bias.

Once the redshift distribution is known (or the uncertainties appropriately marginalized over), theoretical modeling of the signal on intermediate to small scales is the next challenge. Non-linear corrections to both clustering and bias become important at  $\ell$  of few hundred, where the statistical  $S/N$  is still large in each bandpower. This implies that even if  $dN/dz$  were known perfectly, our ability to extract cosmological information could still be limited by our theoretical models. We defer consideration of modeling the signal to future work [25].

In conclusion, we believe that the cross-correlations presented here are an extremely sensitive probe of late-time cosmology. A spectroscopic followup of a subsample of the sources as well as improved modeling of intermediate and small scales can lead to sub-percent measurement, with important possible applications for tests of gravity, measurement of neutrino masses and the properties of Dark Energy.

## Acknowledgments

We thank David Alonso, Enea Di Dio, Yu Feng, Julien Guy, Colin Hill, Ellie Kitanidis, Alexie Leauthaud, Thibaut Louis, Emmanuel Schaan, David Schlegel, Uros Seljak, Blake Sherwin, Zachary Slepian, David Spergel, Katherine Suess and Michael Wilson for very useful discussions. S.F. is supported by the Physics Division at Lawrence Berkeley National Laboratory. M.W. is supported by the U.S. Department of Energy and by NSF grant number 1713791. This research used resources of the National Energy Research Scientific Computing Center (NERSC), a U.S. Department of Energy Office of Science User Facility operated under Contract No. DE-AC02-05CH11231. This work made extensive use of the NASA Astrophysics Data System and of the `astro-ph` preprint archive at [arXiv.org](https://arxiv.org).

## A Spectroscopic followup

A direct measurement of  $dN/dz$  with smaller errors than the COSMOS cross-match  $dN/dz$  would allow for improved modeling of the unWISE samples and better control of systematic errors. Even with improved cross-match  $dN/dz$ , we would still require the photometric-spectroscopic cross-correlations to determine  $b_{\text{lin}}(z)$ , but we could greatly improve the simple HOD modeling in Appendix B and Fig. 16, allowing for better understanding of  $b_{\text{lin}}(z)$  and potentially better control of systematics such as nonlinear bias evolution. With observations in several fields, we could also better understand the variation in  $dN/dz$  on the sky. Finally, we could better understand the impact of blending in our sample by re-targeting both (or all) galaxies blended together by the  $6''$  WISE PSF.

If the errors on  $dN/dz$  were much smaller than the errors on the photometric-spectroscopic clustering measurement, we could neglect  $dN/dz$  errors and better model the unWISE galaxy population. This is not the case in Fig. 16; at  $z < 0.2$  and  $z \sim 0.5$  in the blue sample, the error from uncertain  $dN/dz$  (gray band) is larger than the statistical error on the clustering (blue errorbars). However, this is driven by the HSC-derived cosmic variance correction, which is a factor of 3.8 for the blue sample (Section 5.1). If instead of measuring  $dN/dz$  on a single field, we measured  $dN/dz$  in multiple fields spread across the sky, the errors would be dominated by Poisson rather than cosmic variance, and no such correction would be necessary. Indeed, if we divide out this correction in the  $dN/dz$  errors in Figure 16, we find that  $dN/dz$  errors are at most 80% of the statistical errors for blue and green (peaking at  $z \sim 0.3 - 0.5$ ); for red, the  $dN/dz$  errors are larger at low redshift, 150% of the statistical errors at  $z \sim 0.5$ . Scaling from the number of galaxies with secure COSMOS redshifts (5557, 3024, and 164 for blue, green and red), we estimate that achieving  $dN/dz$  errors that are at most 50% of the statistical errors will require 14000, 7500, and 1500 spectra for the blue, green and red samples. However, a smaller effort focused solely at low redshift could be just as effective for the red sample, since the low redshift tail is much more uncertain than the higher redshift  $dN/dz$ .

By measuring  $dN/dz$  across multiple fields, a spectroscopic followup program could constrain variations in  $dN/dz$  on the sky. Using the standard deviation of the COSMOS cross-match  $dN/dz$ , we estimate that we could measure a 5% shift in the mean  $dN/dz$  at  $3\sigma$  with 1000 spectra per field for both the blue and green samples. For the red sample, with 400 spectra per field we could measure a 10% shift at  $3\sigma$ .

While the full unWISE sample only has infrared fluxes, by cross-matching to COSMOS we can determine the optical colors and properties of unWISE. In Figure 10, we show the distribution of Subaru  $i^+$  for the unWISE galaxies, and the relationship between  $i^+$  and the WISE bands. For the blue sample a 90% completeness is achieved at  $i^+ \simeq 22$  while for the green and red samples 90% completeness occurs at  $i^+ \simeq 24$ .

We also show the stellar mass and star formation rates of unWISE galaxies from COSMOS broad-band photometry. All three unWISE samples have similar stellar masses (with  $\log_{10}(M/M_{\odot}) = 10.80, 10.78, \text{ and } 10.87$  for the blue, green and red samples) but the star-formation rates of the green and red samples ( $\log_{10} \text{SFR}/M_{\odot}\text{yr}^{-1} = 1.03, 1.61$ ) are significantly higher than the star-formation rate of the blue sample ( $\log_{10} \text{SFR}/M_{\odot}\text{yr}^{-1} = 0.12$ ).

Some of the galaxies in the unWISE samples have been observed in the VVDS survey [96] using VIMOS on VLT, allowing us to both better characterize the galaxy samples and understand the feasibility of spectroscopic followup. The VVDS-Deep survey has a simple selection function, uniformly targeting galaxies at  $17.5 < I < 24$ . Not every  $17.5 < I < 24$

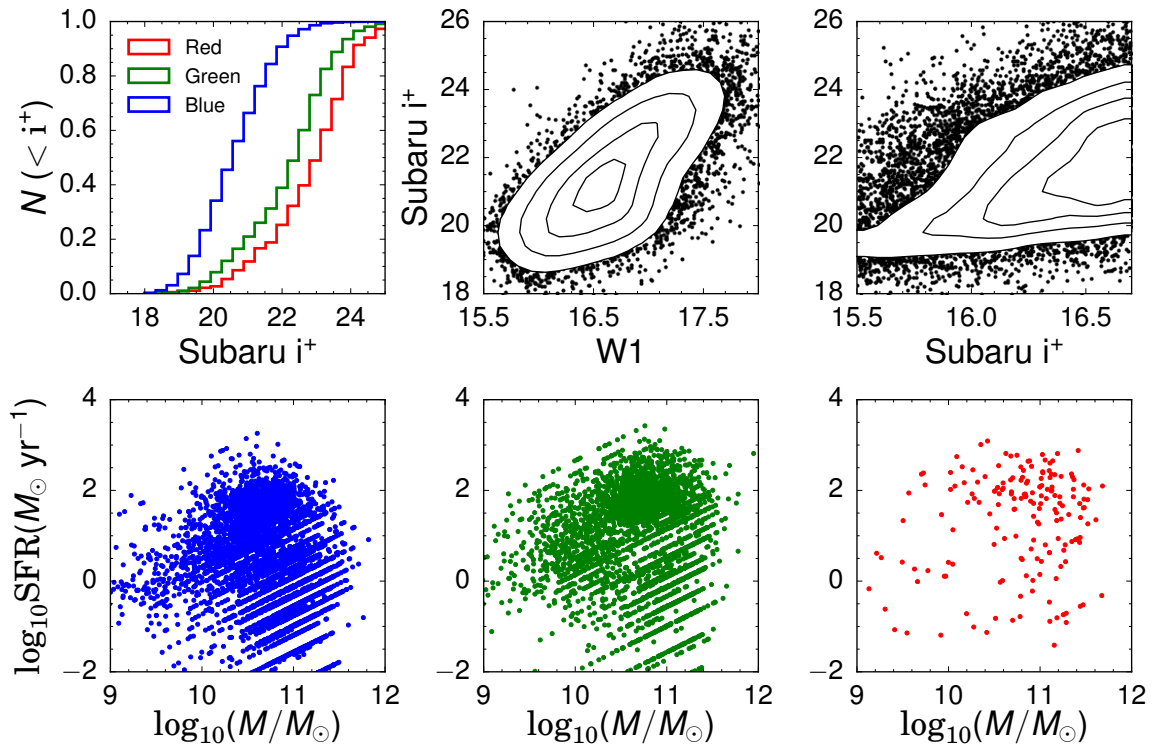


**Figure 10.** *Top left:* Distribution of Subaru  $i^+$  magnitudes (“mag\_auto,” measured in flexible elliptical apertures, as in ref. [95]) from unWISE matched to COSMOS. *Top center and right:* Subaru  $i^+$  versus WISE W1 and W2 magnitudes for the combined red, green and blue samples in COSMOS. We show 20%, 40%, 60% and 80% iso-contours of the cumulative distribution function (Gaussian smoothed with  $\sigma = 1$  mag) of galaxies in  $i^+$  and W1/W2. *Bottom:* Distribution of stellar mass and star formation rate for each of the three samples, from COSMOS broad-band photometry.

galaxy is targeted; to determine the completeness of the unWISE galaxies in VVDS, we must divide the number of matches by the VVDS targeting selection rate (typically 20-30%) and then compare to the number of unWISE galaxies lying within the VVDS spectroscopic mask.<sup>25</sup> We find 444, 261 and 13 VVDS matches to the blue, green and red samples (418, 191 and 10 with high confidence redshifts, ZFLAGS  $\geq 2$ ), implying 101.3%,<sup>26</sup> 89.6% and 70.0% of the blue, green and red samples yield a VVDS spectrum. This agrees well with the fraction of galaxies with  $I < 24$ , which is 99.6% (91.8%, 84.5%) for the three samples, implying that within the range of galaxies that could have been targeted, 97.8%, 69.0% and 59.4% of blue, green and red galaxies received a high-confidence VVDS redshift. VVDS-Deep exposure times are 4.5 hr on a  $R \sim 230$  spectrograph, suggesting that spectroscopic followup of the unWISE samples is feasible on 8-10 m class telescopes (and perhaps smaller telescopes for the brighter blue sample).

We also incorporate galaxies from the VVDS UltraDeep survey, which includes 12, 19,

<sup>25</sup>As with the COSMOS matches, we additionally remove VVDS galaxies with Spitzer-SWIRE [97]  $4.5 \mu\text{m}$  magnitude  $> 19.2$  (18.7 for red sample), although relatively few VVDS galaxies have SWIRE matches so this cut makes little difference.

<sup>26</sup>Completeness higher than 100% likely indicates that the targeting selection rate is somewhat underestimated.

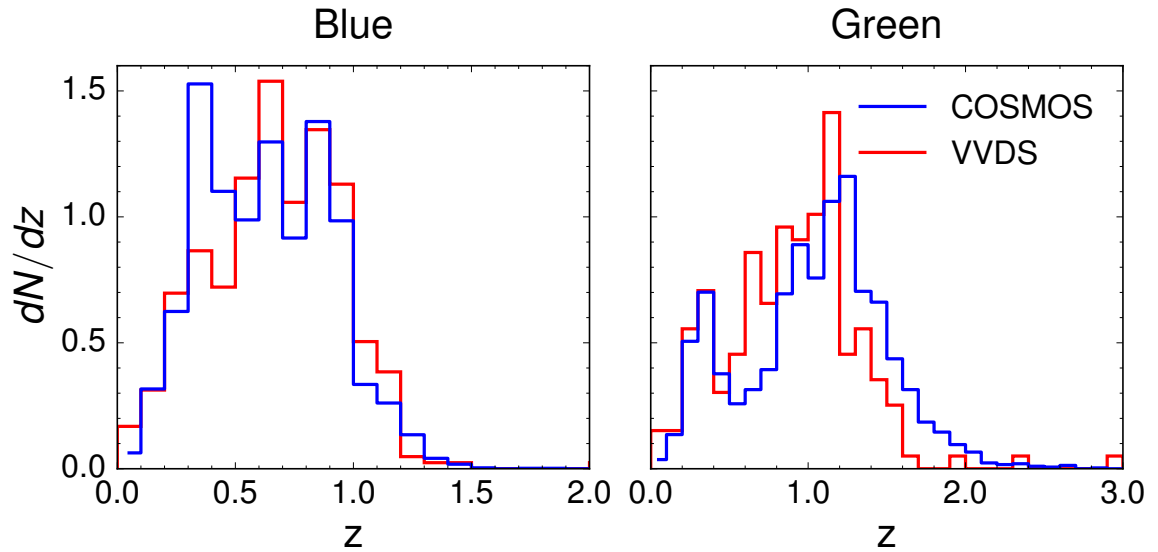


**Figure 11.** Comparison of  $dN/dz$  for COSMOS photometric (blue) and VVDS spectroscopic (red) matches for the blue and green samples (including spectra from VVDS-Deep and VVDS-UltraDeep). The red sample has too few VVDS matches to compare the two  $dN/dz$ . While VVDS is largely complete for the blue sample, incompleteness at the faint, high redshift end of the green sample may bias  $dN/dz$  relative to COSMOS.

and 1 galaxies from the blue, green and red samples (10, 11, and 1 with ZFLAGS  $\geq 2$ ). The redshift distribution of blue galaxies with redshifts from VVDS is quite similar to the COSMOS  $dN/dz$  (Figure 11); for the green sample, the VVDS  $dN/dz$  is suppressed relative to COSMOS at  $z > 1.6$ , possibly because of increased redshift failures at high redshifts where the [OII] line redshifts beyond the red end of the spectrograph.

We display three spectra from each sample in Figure 12, representing each sample at low, medium and high redshift. Blending presents a similar challenge for the VVDS cross-match as for COSMOS, so we only display galaxies that are well-isolated in optical imaging. Due to the paucity of red spectra, the red sources at  $z = 0.477$  and  $z = 2.27$  are blends, although in both cases only one of the two potential optical matches has a VVDS spectrum.

In Figure 13, we plot the distribution of redshift and [OII] 3727 Å EW for the green and blue samples from VVDS spectra, as well as  $D_n(4000)$  versus [OII] 3727 Å EW, to separate star-forming from quiescent galaxies as in ref. [98]. We find median [OII] 3727 Å EW of 6.4 (11.8) Å in emission for the blue (green) sample, and from the star-forming versus quiescent cut from ref. [98], 29.0% (60.3%) of blue (green) galaxies are star-forming.

## B Simple HOD model for unWISE samples

When computing  $dN/dz$  using cross-correlations we assumed a scale-independent bias, and we found that in order for the cross-match and cross-correlation  $dN/dz$  to match, the biases needed to evolve relatively rapidly with redshift. In this Appendix we check whether this assumption and its implications are consistent with expectations from simple models of the manner in which galaxies populate dark matter halos.

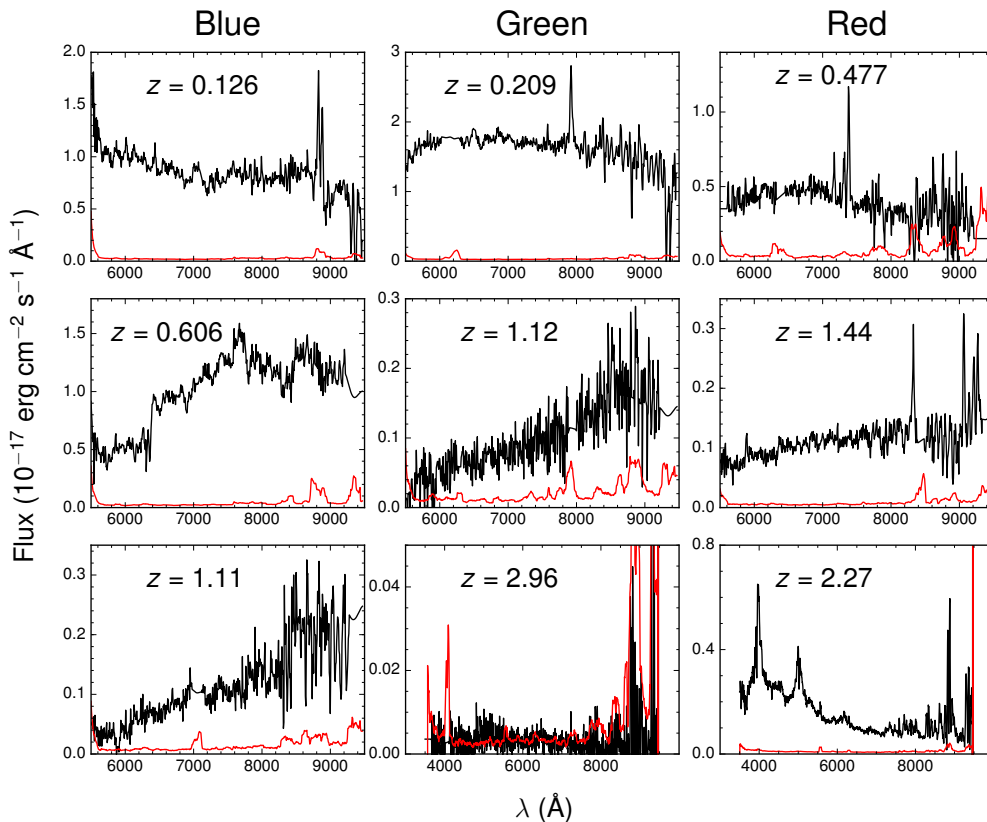


**Figure 12.** VVDS spectra from each of the three unWISE samples, with spectra in black and noise in red. For each of the three samples we display galaxies representative of the low, medium, and high portion of the redshift distribution. The highest redshift green and red galaxies are from VVDS-UltraDeep, which took spectra in both the blue and red grisms of VIMOS; all other galaxies are from VVDS-Deep, which only observed using the red grism.

A scale-independent bias is likely to be true on large, linear scales, but the extent to which this approximation is valid on the scales used in the  $dN/dz$  analysis is unclear. If the bias is scale-dependent, the redshift evolution of  $b_{\text{sml,p}}$  may not match the redshift evolution of  $b_{\text{lin,p}}$  (relevant for  $C_\ell^{kg}$  and  $C_\ell^{gg}$ ), potentially introducing a systematic bias. To investigate this issue we model the unWISE galaxies using a simple HOD applied to dark matter halos in  $N$ -body simulations, allowing us to study the scale and redshift dependence of the unWISE galaxy bias. Since our goal is modest, we simply use a 1-parameter family<sup>27</sup> of HODs based on ref. [101] with

$$\langle N_{\text{cen}} \rangle = \frac{1}{2} \left[ 1 + \text{erf} \left( \frac{\log_{10} M - \log_{10} M_{\text{cut}}}{\sqrt{2} \sigma_{\log_{10} M}} \right) \right] \quad ; \quad \sigma_{\log_{10} M} = 0.25 \quad (\text{B.1})$$

and

$$\langle N_{\text{sat}} \rangle = \left[ \frac{M - 0.1 M_{\text{cut}}}{15 M_{\text{cut}}} \right]^{0.8} . \quad (\text{B.2})$$

<sup>27</sup>There is some evidence that HOD parameters scale approximately universally with number density, e.g. ref. [99]. A similar assumption is at the root of the ‘SHAM’ approximation [100].

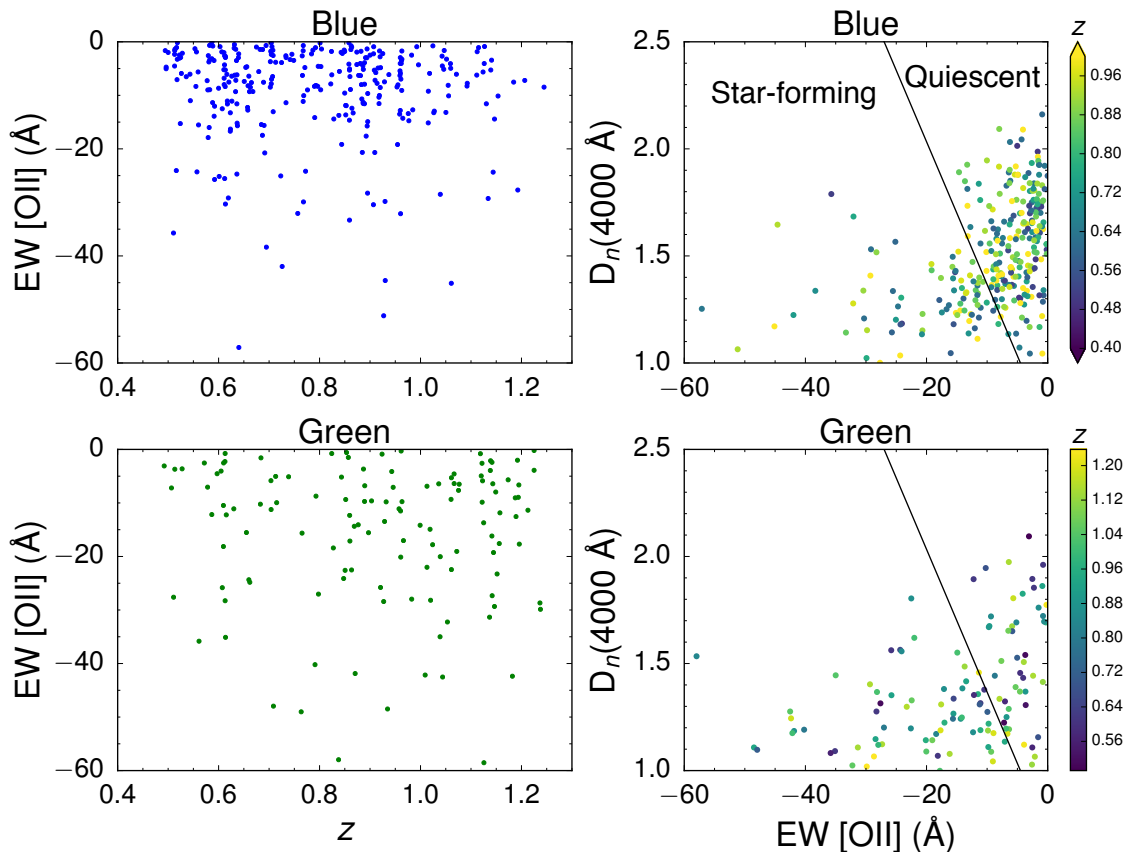


**Figure 13.** *Left:* From VVDS spectra, distribution of [OII] 3727 Å EW versus redshift for the blue sample (top) and green sample (bottom). *Right:* Distribution of [OII] 3727 Å EW versus  $D_n(4000)$  to separate star forming and quiescent galaxies as in ref. [98]. Points are color-coded to represent redshift.

The values of  $\sigma_{\log_{10}M}$ , and the power-law index and denominator in  $\langle N_{\text{sat}} \rangle$  are typical of magnitude-selected galaxy samples and our final results are not very sensitive to them. The number density and large- and small-scale biases  $b_{\text{HOD}}(z)$  can then be computed as a function of  $\log_{10}M_{\text{cut}}$ . We compute the comoving number density of unWISE galaxies from the COSMOS cross-match  $dN/dz$  (Section 5.1) and choose the cutoff mass  $M_c$  to match the abundance of each sample at all redshifts. The results are given in Table 8.

To reduce scatter, we averaged the results from halo catalogs generated from 4 simulations, each with  $1280^3$  particles in a  $640 h^{-1}\text{Mpc}$  box, assuming  $\Lambda\text{CDM}$  with parameters matching the Planck 2018 best fit model [102]. We consider friends-of-friends halos with linking length 0.168 of the mean interparticle spacing at four representative redshifts  $z = 0.41, 1.00, 1.27$  and  $1.78$ . At each redshift we adjusted  $\log_{10}M_{\text{cut}}$  as in Table 8 and measured the real-space correlation function by direct pair counting of the halos, hence obtaining the projected correlation function,  $w_p(R)$ . We define the real-space bias as a function of scale

$$b(R) = \sqrt{w_p(R)/w_{p,\text{HF}}(R)} \quad (\text{B.3})$$

| $z_{\min}$ | $z_{\max}$ | LOWZ               |            | CMASS              |            | $z_{\min}$ | $z_{\max}$ | eBOSS Q            |            | BOSS Q             |            |
|------------|------------|--------------------|------------|--------------------|------------|------------|------------|--------------------|------------|--------------------|------------|
|            |            | $b_{\text{sml},s}$ | $\sigma_b$ | $b_{\text{sml},s}$ | $\sigma_b$ |            |            | $b_{\text{sml},s}$ | $\sigma_b$ | $b_{\text{sml},s}$ | $\sigma_b$ |
| 0.00       | 0.05       | 1.34               | 0.0381     |                    |            | 0.00       | 0.20       |                    |            |                    |            |
| 0.05       | 0.10       | 1.37               | 0.0077     |                    |            | 0.20       | 0.40       |                    |            |                    |            |
| 0.10       | 0.15       | 1.52               | 0.0037     | 1.36               | 0.2698     | 0.40       | 0.60       |                    |            |                    |            |
| 0.15       | 0.20       | 1.73               | 0.0045     | 2.82               | 0.2615     | 0.60       | 0.80       |                    |            |                    |            |
| 0.20       | 0.25       | 1.89               | 0.0039     | 1.54               | 0.0796     | 0.80       | 1.00       | 1.72               | 0.2803     |                    |            |
| 0.25       | 0.30       | 2.01               | 0.0018     | 2.11               | 0.1489     | 1.00       | 1.20       | 2.03               | 0.0851     |                    |            |
| 0.30       | 0.35       | 2.01               | 0.0021     | 1.99               | 0.1054     | 1.20       | 1.40       | 2.05               | 0.0759     |                    |            |
| 0.35       | 0.40       | 2.06               | 0.0019     | 2.24               | 0.1674     | 1.40       | 1.60       | 2.35               | 0.0683     |                    |            |
| 0.40       | 0.45       | 2.25               | 0.0017     | 2.05               | 0.0020     | 1.60       | 1.80       | 2.32               | 0.0992     |                    |            |
| 0.45       | 0.50       | 2.46               | 0.0079     | 2.08               | 0.0006     | 1.80       | 2.00       | 2.89               | 0.1004     |                    |            |
| 0.50       | 0.55       |                    |            | 2.06               | 0.0008     | 2.00       | 2.20       | 2.87               | 0.1548     |                    |            |
| 0.55       | 0.60       |                    |            | 2.17               | 0.0007     | 2.20       | 2.40       |                    |            | 4.33               | 0.0808     |
| 0.60       | 0.65       |                    |            | 2.22               | 0.0010     | 2.40       | 2.60       |                    |            | 3.72               | 0.1394     |
| 0.65       | 0.70       |                    |            | 2.39               | 0.0022     | 2.60       | 2.80       |                    |            | 4.27               | 0.3772     |
| 0.70       | 0.75       |                    |            | 2.52               | 0.0090     | 2.80       | 3.00       |                    |            | 4.30               | 1.2109     |
| 0.75       | 0.80       |                    |            | 2.73               | 0.0872     | 3.00       | 3.20       |                    |            | 4.30               | 1.1164     |
|            |            |                    |            |                    |            | 3.20       | 3.40       |                    |            | 5.33               | 1.9984     |

**Table 7.** Bias of the spectroscopic samples and the 1- $\sigma$  error bar, as defined in Equation 5.9.

| $z$  | Blue                        |   | Green                       |   | Red                         |   |
|------|-----------------------------|---|-----------------------------|---|-----------------------------|---|
|      | $\log_{10}(M_{\text{cut}})$ | Abundance<br>( $h^3 \text{ Mpc}^{-3}$ ) | $\log_{10}(M_{\text{cut}})$ | Abundance<br>( $h^3 \text{ Mpc}^{-3}$ ) | $\log_{10}(M_{\text{cut}})$ | Abundance<br>( $h^3 \text{ Mpc}^{-3}$ ) |
| 0.41 | 12.25                       | $3.44 \times 10^{-3}$                   | 13.00                       | $5.57 \times 10^{-4}$                   | 13.50                       | $1.39 \times 10^{-4}$                   |
| 1.00 | 12.50                       | $1.43 \times 10^{-3}$                   | 12.75                       | $7.19 \times 10^{-4}$                   | 13.50                       | $6.55 \times 10^{-5}$                   |
| 1.27 | 13.25                       | $1.11 \times 10^{-4}$                   | 12.75                       | $5.71 \times 10^{-4}$                   | 13.50                       | $4.26 \times 10^{-5}$                   |
| 1.78 |                             |   | 13.00                       | $5.57 \times 10^{-4}$                   | 13.50                       | $1.39 \times 10^{-4}$                   |

**Table 8.** Halos populated with the HOD of Eq. B.1 and Eq. B.2, at four output times. All HODs use  $\sigma_{\log_{10} M} = 0.25$  decades, and  $\log_{10} M_{\text{cut}}$  is then selected to roughly match the abundance of each unWISE sample at the specified redshift.

define  $b_{\text{sml}}$  with the same  $R^{-1}$  weighting as in Eq. 5.2:

$$b_{\text{sml}} = \int_{r_{\min}}^{r_{\max}} dR R^{-1} b(R) \Big/ \int_{r_{\min}}^{r_{\max}} dR R^{-1} \quad (\text{B.4})$$

and define  $b_{\text{lin}} \equiv b(r = 40 h^{-1} \text{Mpc})$ .

We find only mild departures from scale-independent bias at  $2.5 < r_p < 10 h^{-1} \text{Mpc}$ , but more significant deviations at smaller scales, in qualitative agreement with the spectroscopic cross-correlations (Figure 14). From the  $N$ -body autocorrelations, we find  $b_{\text{sml}}/b_{\text{lin}} = 1.153$  for red at  $z = 1.78$ , the most massive and highest-redshift sample (Figure 15). To interpolate between the four measured points, we use a function of the form  $b_{\text{sml}}/b_{\text{lin}} = 1 + Az^2$ , with  $A = 0.1$  for red and  $A = 0.05$  for green and blue. We then conservatively assume that the true value of  $A$  lies between 0 and  $2A$ , accounting for the substantial uncertainty in the halo occupation of the unWISE galaxies and the crudeness of our model. Further, the scale-dependence of the bias is somewhat stronger in the  $N$ -body autocorrelations than in the data, implying that our scale-dependent bias corrections are therefore somewhat conservative.

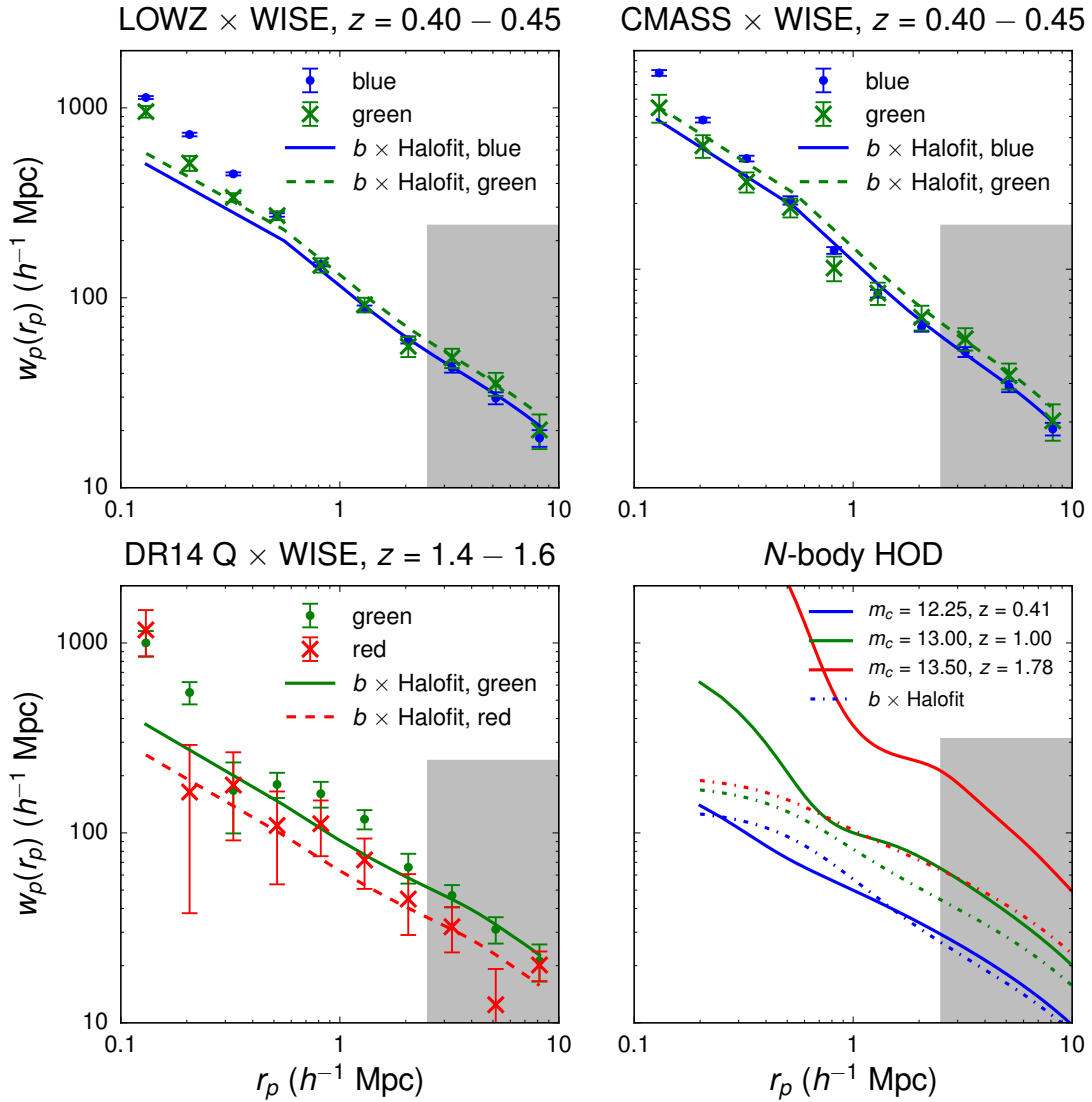


**Figure 14.** Cross-correlations between spectroscopic tracers and the unWISE galaxy samples, compared to a scale-independent bias times nonlinear correlation function fit to the points with  $2.5 < r_p < 10 h^{-1}$  Mpc (shaded region). Deviations from scale-independent bias are seen at  $r_p < 2.5 h^{-1}$  Mpc, justifying our decision to use  $2.5 < r_p < 10 h^{-1}$  Mpc for the cross-correlation redshifts. *Lower right:* autocorrelation of galaxies populating halos in an  $N$ -body simulation according to Eq. B.1 and B.2 with  $\sigma_{\log_{10} M} = 0.25$  decades. Redshifts and number densities are chosen to be roughly representative of the three unWISE samples. Since the lower right panel is an autocorrelation ( $\propto b_{\text{unWISE}}^2$ ) while the other panels are cross-correlations ( $\propto b_{\text{unWISE}}$ ), it has a much stronger scale-dependent bias at  $z \sim 1.5$  (since the unWISE galaxies have larger and thus more scale-dependent bias than the quasars).

To assess the compatibility of the cross-correlation and cross-match  $dN/dz$ , we compare the bias evolution of galaxies in the HOD,  $b_{\text{HOD}}(z)$ , to the observed bias evolution of the unWISE galaxies,  $b_{\text{sml,p}}(z)$ , in Figure 16. Using Equation 5.4, the COSMOS  $dN/dz$ , and  $s$  from Appendix C, we fit  $b_{\text{sml,p}}(z)$  to  $w(\theta)$  between 2.5 and 10  $h^{-1}$  Mpc. Consistency

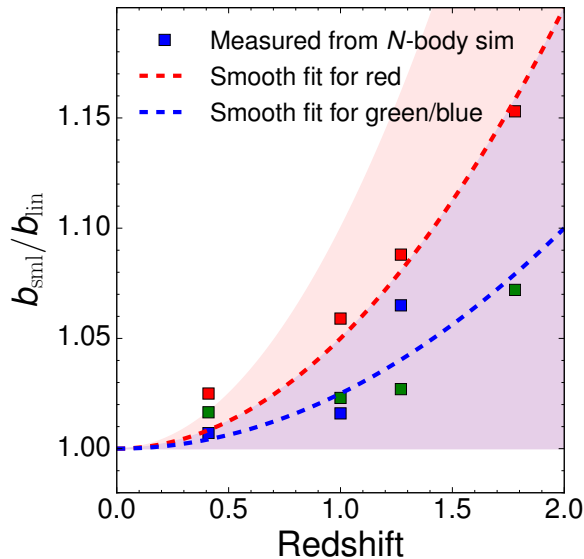


**Figure 15.** Ratio between  $b_{\text{sml}}$  and  $b_{\text{lin}}$  for HODs matched to the three unWISE samples at four representative redshifts in the  $N$ -body simulation. Dashed lines give interpolating functions  $b_{\text{sml}}/b_{\text{lin}} = 1 + Az^2$  with separate values of  $A$  for red and blue/green; shaded regions represent uncertainty on  $A$ , accounting for uncertainty in the halo occupation of the unWISE galaxies.

between the cross-match  $dN/dz$  and photometric-spectroscopic clustering (from which the cross-correlation  $dN/dz$  is derived) requires a steeply evolving galaxy bias (colored lines in Figure 16). In fact, the simple abundance-matched HOD yields a galaxy bias that is nearly as steep (Figure 16). We compare  $b_{\text{sml,p}}(z)$  to  $b_{\text{HOD}}(z)$  using the HOD above and one of three different mass function/mass-bias relationships (Tinker et al., [103, 104], Sheth, Mo and Tormen [105, 106], and Comparat et al. [107]). We consider both statistical errors on  $b_{\text{sml,p}}$  from errors on the cross-correlation (errorbars in Figure 16), and errors on  $b_{\text{sml,p}}$  from the uncertain  $dN/dz$  (gray band, giving 16th-84th percentile range from 100 draws from  $dN/dz$ ). While the uncertainty in  $dN/dz$  will also affect the bias evolution of the abundance-matched halos by changing their comoving number density, this effect is smaller than the impact of uncertain  $dN/dz$  on  $b_{\text{sml,p}}(z)$  because the bias is a shallow function of halo mass and thus number density.

For the blue sample, and for the red and green samples at  $z > 1$ , the measured bias evolution roughly agrees with the HOD prediction within the uncertainty from  $dN/dz$ . At  $z < 1$ , the bias of the red and green samples is significantly lower than the expectation from the HOD. However, both the red and green samples are bimodal, and it is possible that their low-redshift tails are not well-described by the HOD above. For instance, the low-redshift tails could consist of star-forming galaxies occupying halos with a duty cycle well below unity, such that at fixed abundance, the cutoff halo mass is much lower than the HOD above would predict, thus lowering the bias.

The rough agreement between  $b_{\text{sml,p}}(z)$  and  $b_{\text{HOD}}(z)$  for the abundance-matched halos shows that the combination of cross-correlation and cross-match redshifts yields a reasonable bias evolution. This result justifies our use of both the cross-correlation and cross-match redshifts in modelling  $C_\ell^{rg}$  and  $C_\ell^{gg}$ , as it suggests they are consistent with each other.

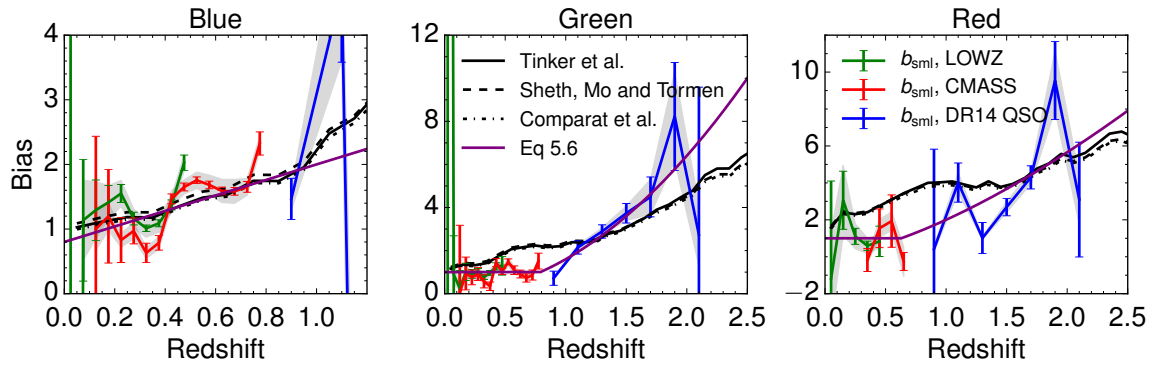


**Figure 16.** Bias, derived from  $w(\theta)$  at  $2.5 < r < 10 h^{-1}\text{Mpc}$  using Equation 5.4 and the COSMOS cross-match redshift distribution. Colored lines give the measured bias; black lines give the bias evolution for an HOD abundance-matched to the density of the WISE samples, with different line styles corresponding to different bias-number density prescriptions from the literature. Errorbars on the colored lines are from measurement errors on  $w(\theta)$ ; the gray bands give the additional uncertainty from uncertain  $dN/dz$ , quantified by the 16th-84th percentile range from 100 samples of  $dN/dz$ . All fits to clustering include magnification bias using the fiducial values in Table 1 and Fig. 18.

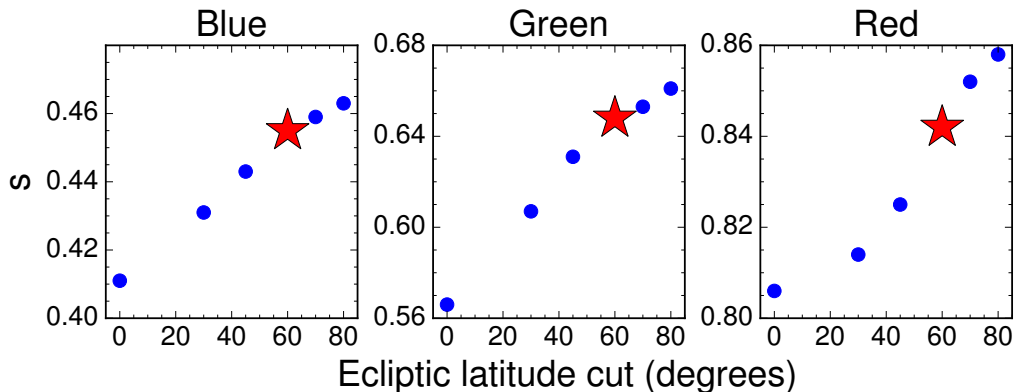


**Figure 17.** Dependence of  $s$  for the unWISE samples on ecliptic latitude. Each point shows  $s(\lambda_{\min})$  measured using galaxies with ecliptic  $|\lambda| > \lambda_{\min}$ . The starred point gives the fiducial value of  $s$ , using  $\lambda_{\min} = 60^\circ$ .

### C Response of the number density to magnification bias

The amplitude of the magnification bias term depends on the response of the galaxy density to magnification bias,  $s \equiv d \log_{10} N/dm$ , at the limiting magnitude of the survey. Since the completeness of WISE drops over a relatively large range, measurements of  $s$  are affected by incompleteness in WISE. This can be mitigated by restricting the sample to high ecliptic latitude, where the greater depth of coverage results in a fainter limiting magnitude.

Since the WISE galaxies are selected via a magnitude-dependent color cut, one cannot simply histogram them in W2 to determine  $s$ . Instead, we compute  $s$  by shifting the magnitudes of all WISE objects by 0.02 magnitudes and re-applying our selection criteria.

In Figure 17, we show  $s$  as a function of  $\lambda_{\min}$ , where we sequentially remove all galaxies with  $|\lambda| < \lambda_{\min}$ . We set the fiducial value of  $s$  at  $\lambda_{\min} = 60^\circ$ .

We also require  $s$  for each of the spectroscopic samples in order to subtract the magni-

fication bias contribution from  $\bar{w}_{\text{sp}}$ . We measure  $s$  by making all galaxies or quasars in the sample fainter by 0.1 magnitudes, applying the relevant selection criteria and measuring the change in number counts.

For LOWZ and CMASS, we use the color cuts described in Ref. [79]. This procedure assumes that every galaxy in the spectroscopic sample with perturbed photometry was also in the original sample; this is true for both CMASS and LOWZ (see Figures 3 and 4 in Ref. [79] for color-magnitude plots for LOWZ and CMASS, respectively).

DR12 quasars are selected as point sources with  $g < 22$  or  $r < 21.85$ ,  $i > 17.8$ , and XDQSO “mid- $z$ ” quasar probability (i.e. probability the object is a  $2.2 < z < 3.5$  quasar)  $> 0.424$  [108, 109]. When we make the quasars fainter by 0.1 magnitudes, we estimate the number of quasars that would be spuriously categorized as extended using the completeness of SDSS star-galaxy separation as a function of  $r$  band magnitude[110].<sup>28</sup> Unlike the color cuts used for the BOSS galaxies, with the more complicated XDQSO color cut it is possible that quasars could be excluded from the original targeting but included when the photometry is made fainter by 0.1 magnitudes. To estimate the occurrence of such objects, we use the BOSS BONUS sample of non-uniformly-selected quasars, which are not suitable for quasar clustering analyses but are  $\sim 2\times$  as abundant as the CORE sample that we do use. Since BONUS quasars are not selected using XDQSO, they may have mid- $z$  quasar probability  $< 0.424$  but “scatter into” our fainter sample.

For DR14 quasars, we follow a similar procedure as for DR12 quasars, applying the selection criteria of Ref. [85]. However, we lack a similarly deep quasar sample (like BONUS in DR12) to determine the number of quasars that scatter into the DR14 selection criteria when the quasar photometry becomes fainter. Based on the number of quasars that scattered into the DR12 quasar selection, we estimate an additional systematic error of  $\Delta s \sim 0.1 - 0.2$  for the DR14 quasars.

We plot the resulting  $s$  in Figure 18, and use them to remove magnification bias from  $\bar{w}$ . For  $z$  beyond the range shown in Figure 18, we assume  $s$  is a constant function, using the nearest point for which we have a measurement of  $s$ .

## D Galaxy-galaxy cross spectra

In Figure 19 we show the cross-spectra between the different galaxy samples. We use the fiducial cross-correlation  $dN/dz$  and  $b_{\text{cross}}^{\text{eff}}$  for the theory calculation. Additionally, we fit a shot-noise term, and find good agreement between the expectation and the data once the uncertainty on  $dN/dz$  is taken into account. For red cross blue the shot noise term is negligible, but for blue cross green and blue cross red, we find shot noise values of  $5.46 \times 10^{-9}$  and  $3.63 \times 10^{-8}$ , respectively. Shot noise can arise in a cross-correlation if some of the objects in the two samples occupy the same halo, with density  $\bar{n}_{\text{common}}$ . The cross shot-noise is then given by

$$\text{Shot Noise} = \frac{\bar{n}_{\text{common}}}{\bar{n}_1 \bar{n}_2} \quad (\text{D.1})$$

Using the fitted shot noise for each sample from Table 4, we find  $\bar{n}_{\text{common}} = 92 \text{ deg}^{-2}$  for blue cross green and  $38 \text{ deg}^{-2}$  for green cross red. This implies that 2.7% (4.9%) of the blue (green) sample lives in the same halo as a green (blue) object, and 2.0% (26.0%) of the green (red) sample lives in the same halo as a red (green) object.

<sup>28</sup><https://classic.sdss.org/dr7/products/general/stargalsep.html>

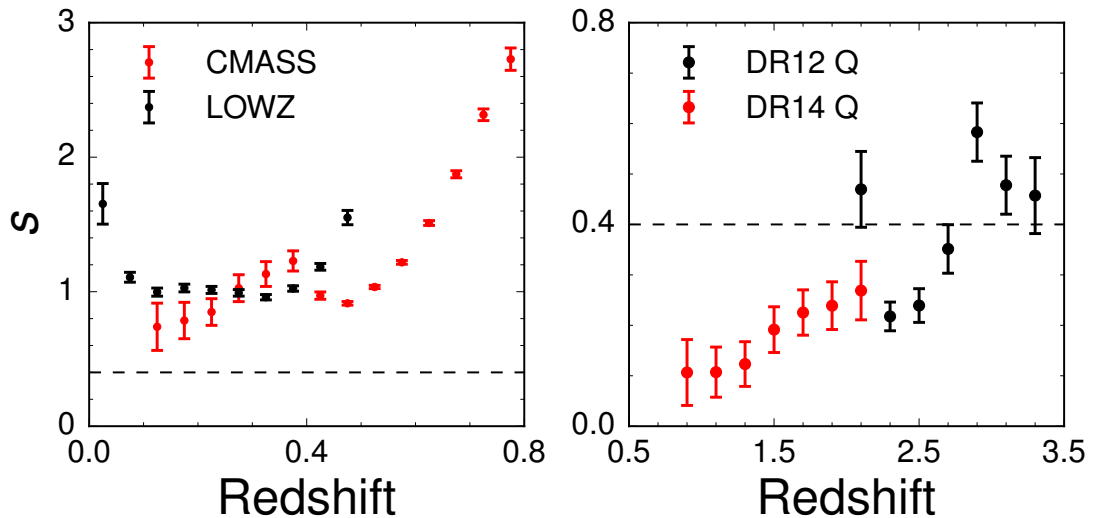


**Figure 18.** Response of galaxy number density to magnification for spectroscopic samples. Error bars are computed as  $\Delta s = (\log_{10} N - \log_{10}(N - \sqrt{N}))/\Delta m$ . Dashed line indicates  $s = 0.4$ , where magnification bias makes no contribution to the observed clustering.

We create a simple “joint HOD” to understand the cross shot-noise. Rather than assume that every halo well above  $M_{\text{cut}}$  hosts a central galaxy, we instead assume that some halos host red centrals and other halos host green centrals; i.e. we multiply  $N_{\text{cen}}$  by  $f_{\text{green}}$  or  $f_{\text{red}}$  where  $f_{\text{green}} + f_{\text{red}} = 1$ , and do not modify  $N_{\text{sat}}$ . We then ask what fraction of red galaxies host a green satellite. If  $f_{\text{green}} = f_{\text{red}} = 0.5$ , we find that 26.3% of red galaxies host at least one green satellite. The common fraction remains similar at 15-25% if we change some aspects of this toy model (i.e. increase  $f_{\text{green}}$  to 0.9; add a linear ramp where halos transition from hosting green galaxies at low redshift to red galaxies at high redshift; or multiply  $N_{\text{sat}}$  by 0.5 for both green and red to preserve the total number of satellites).

## References

- [1] A. Lewis and A. Challinor, *Weak gravitational lensing of the CMB*, *PhysRep* **429** (2006) 1 [[astro-ph/0601594](#)].
- [2] D. Hanson, A. Challinor and A. Lewis, *Weak lensing of the CMB*, *General Relativity and Gravitation* **42** (2010) 2197 [[0911.0612](#)].
- [3] W. Hu, *Power spectrum tomography with weak lensing*, *Astrophys. J.* **522** (1999) L21 [[astro-ph/9904153](#)].
- [4] W. Hu, *Dark energy and matter evolution from lensing tomography*, *Phys. Rev.* **D66** (2002) 083515 [[astro-ph/0208093](#)].
- [5] K. M. Smith, O. Zahn and O. Dore, *Detection of Gravitational Lensing in the Cosmic Microwave Background*, *Phys. Rev.* **D76** (2007) 043510 [[0705.3980](#)].
- [6] C. M. Hirata, S. Ho, N. Padmanabhan, U. Seljak and N. A. Bahcall, *Correlation of CMB with large-scale structure: II. Weak lensing*, *Phys. Rev.* **D78** (2008) 043520 [[0801.0644](#)].
- [7] B. D. Sherwin et al., *The Atacama Cosmology Telescope: Cross-Correlation of CMB Lensing and Quasars*, *Phys. Rev.* **D86** (2012) 083006 [[1207.4543](#)].

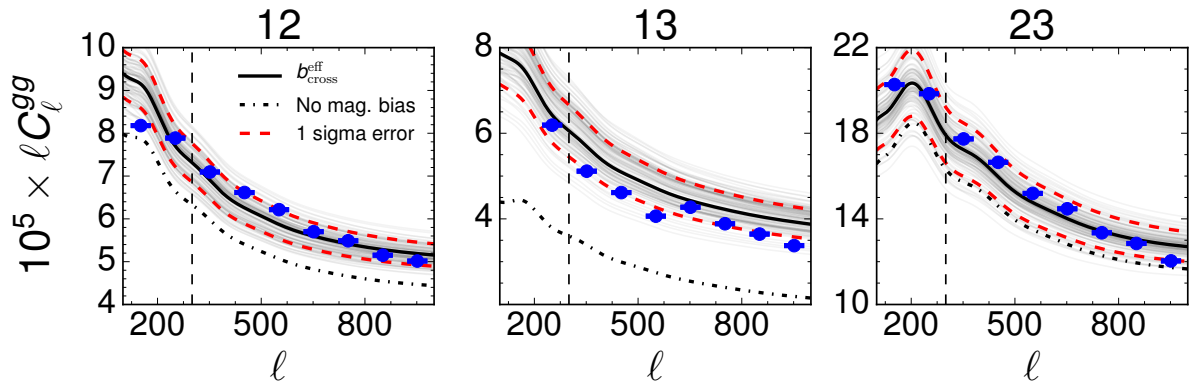


**Figure 19.** Galaxy-galaxy cross-spectra between the different samples. The solid black line gives the predicted theory curve using  $b_{\text{cross}}^{\text{eff}}$ , and the dot-dashed black line gives the predicted theory curve with no magnification bias included. Gray lines show  $C_{\ell}^{gg}$  from 100 realizations of  $dN/dz$  (with bias modified from the best-fit  $b_{\text{cross}}^{\text{eff}}$  in Table 4 to fit  $C_{\ell}^{gg}$  for a given  $dN/dz$ ); and dashed red lines show  $1\sigma$  uncertainty in  $C_{\ell}^{gg}$ , with contributions both from uncertain  $dN/dz$  and from statistical errors on  $b_{\text{cross}}^{\text{eff}}$ . Uncertainty on  $C_{\ell}^{gg}$  for  $dN/dz$  from the two halves of the sky is comparable to the  $1\sigma$  uncertainty. In all cases, a cross shot-noise term is fit to the data and also included in the theory curves.

- [8] L. E. Bleem et al., *A Measurement of the Correlation of Galaxy Surveys with CMB Lensing Convergence Maps from the South Pole Telescope*, *Astrophys. J.* **753** (2012) L9 [[1203.4808](#)].
- [9] Planck Collaboration, P. A. R. Ade, N. Aghanim, C. Armitage-Caplan, M. Arnaud, M. Ashdown et al., *Planck 2013 results. XVII. Gravitational lensing by large-scale structure*, *A&A* **571** (2014) A17 [[1303.5077](#)].
- [10] Y. Omori and G. Holder, *Cross-Correlation of CFHTLenS Galaxy Number Density and Planck CMB Lensing*, *arXiv e-prints* (2015) arXiv:1502.03405 [[1502.03405](#)].
- [11] R. Allison, S. N. Lindsay, B. D. Sherwin, F. de Bernardis, J. R. Bond, E. Calabrese et al., *The Atacama Cosmology Telescope: measuring radio galaxy bias through cross-correlation with lensing*, *MNRAS* **451** (2015) 849 [[1502.06456](#)].
- [12] F. Bianchini, P. Bielewicz, A. Lapi, J. Gonzalez-Nuevo, C. Baccigalupi, G. de Zotti et al., *Cross-correlation between the CMB Lensing Potential Measured by Planck and High- $z$  Submillimeter Galaxies Detected by the Herschel-Atlas Survey*, *ApJ* **802** (2015) 64 [[1410.4502](#)].
- [13] E. Baxter, J. Clampitt, T. Giannantonio, S. Dodelson, B. Jain, D. Huterer et al., *Joint measurement of lensing-galaxy correlations using SPT and DES SV data*, *MNRAS* **461** (2016) 4099 [[1602.07384](#)].
- [14] T. Giannantonio, P. Fosalba, R. Cawthon, Y. Omori, M. Crocce, F. Elsner et al., *CMB lensing tomography with the DES Science Verification galaxies*, *MNRAS* **456** (2016) 3213 [[1507.05551](#)].
- [15] Y. Omori, T. Giannantonio, A. Porredon, E. Baxter, C. Chang, M. Crocce et al., *Dark Energy Survey Year 1 Results: tomographic cross-correlations between DES galaxies and CMB lensing from SPT+Planck*, *arXiv e-prints* (2018) arXiv:1810.02342 [[1810.02342](#)].
- [16] G. A. Marques and A. Bernui, *Tomographic analyses of the CMB lensing and galaxy clustering to probe the linear structure growth*, [1908.04854](#).
- [17] E. F. Schlafly, A. M. Meisner and G. M. Green, *The unWISE Catalog: Two Billion Infrared*

Sources from Five Years of WISE Imaging, *The Astrophysical Journal Supplement Series* **240** (2019) 30 [1901.03337].

- [18] E. L. Wright, P. R. M. Eisenhardt, A. K. Mainzer, M. E. Ressler, R. M. Cutri, T. Jarrett et al., *The Wide-field Infrared Survey Explorer (WISE): Mission Description and Initial On-orbit Performance*, *AJ* **140** (2010) 1868 [1008.0031].
- [19] Gaia Collaboration, T. Prusti, J. H. J. de Bruijne, A. G. A. Brown, A. Vallenari, C. Babusiaux et al., *The Gaia mission*, *A&A* **595** (2016) A1 [1609.04153].
- [20] S. Ferraro, B. D. Sherwin and D. N. Spergel, *WISE measurement of the integrated Sachs-Wolfe effect*, *PRD* **91** (2015) 083533 [1401.1193].
- [21] S. Ferraro, J. C. Hill, N. Battaglia, J. Liu and D. N. Spergel, *Kinematic Sunyaev-Zel'dovich effect with projected fields. II. Prospects, challenges, and comparison with simulations*, *Phys. Rev. D* **94** (2016) 123526 [1605.02722].
- [22] J. C. Hill, S. Ferraro, N. Battaglia, J. Liu and D. N. Spergel, *Kinematic Sunyaev-Zel'dovich Effect with Projected Fields: A Novel Probe of the Baryon Distribution with Planck, WMAP, and WISE Data*, *Phys. Rev. Lett.* **117** (2016) 051301 [1603.01608].
- [23] A. J. Shajib and E. L. Wright, *Measurement of the integrated Sachs-Wolfe effect using the AllWISE data release*, *Astrophys. J.* **827** (2016) 116 [1604.03939].
- [24] Planck Collaboration, N. Aghanim, Y. Akrami, M. Ashdown, J. Aumont, C. Baccigalupi et al., *Planck 2018 results. VIII. Gravitational lensing*, *ArXiv e-prints* (2018) [1807.06210].
- [25] A. Krolewski, S. Ferraro, E. Schlafly and M. J. White, *In Preparation (2019)*, .
- [26] Planck Collaboration, N. Aghanim, Y. Akrami, M. Ashdown, J. Aumont, C. Baccigalupi et al., *Planck 2018 results. VI. Cosmological parameters*, *arXiv e-prints* (2018) arXiv:1807.06209 [1807.06209].
- [27] W. Hu and T. Okamoto, *Mass Reconstruction with Cosmic Microwave Background Polarization*, *ApJ* **574** (2002) 566 [astro-ph/0111606].
- [28] K. M. Górski, E. Hivon, A. J. Banday, B. D. Wand elt, F. K. Hansen, M. Reinecke et al., *HEALPix: A Framework for High-Resolution Discretization and Fast Analysis of Data Distributed on the Sphere*, *ApJ* **622** (2005) 759 [astro-ph/0409513].
- [29] E. Schaan and S. Ferraro, *Foreground-Immune Cosmic Microwave Background Lensing with Shear-Only Reconstruction*, *Phys. Rev. Lett.* **122** (2019) 181301 [1804.06403].
- [30] M. S. Madhavacheril and J. C. Hill, *Mitigating Foreground Biases in CMB Lensing Reconstruction Using Cleaned Gradients*, *Phys. Rev. D* **98** (2018) 023534 [1802.08230].
- [31] A. van Engelen, S. Bhattacharya, N. Sehgal, G. P. Holder, O. Zahn and D. Nagai, *CMB Lensing Power Spectrum Biases from Galaxies and Clusters using High-angular Resolution Temperature Maps*, *Astrophys. J.* **786** (2014) 13 [1310.7023].
- [32] S. J. Osborne, D. Hanson and O. Doré, *Extragalactic Foreground Contamination in Temperature-based CMB Lens Reconstruction*, *JCAP* **1403** (2014) 024 [1310.7547].
- [33] A. Mainzer, J. Bauer, T. Grav, J. Masiero, R. M. Cutri, J. Dailey et al., *Preliminary Results from NEOWISE: An Enhancement to the Wide-field Infrared Survey Explorer for Solar System Science*, *ApJ* **731** (2011) 53 [1102.1996].
- [34] R. M. Cutri, E. L. Wright, T. Conrow, J. W. Fowler, P. R. M. Eisenhardt, C. Grillmair et al., *Explanatory Supplement to the AllWISE Data Release Products*, tech. rep., Nov, 2013.
- [35] A. Mainzer, J. Bauer, R. M. Cutri, T. Grav, J. Masiero, R. Beck et al., *Initial Performance of the NEOWISE Reactivation Mission*, *ApJ* **792** (2014) 30 [1406.6025].
- [36] A. M. Meisner, D. Lang and D. J. Schlegel, *Full-depth Coadds of the WISE and First-year NEOWISE-reactivation Images*, *AJ* **153** (2017) 38 [1603.05664].

- [37] A. M. Meisner, D. Lang and D. J. Schlegel, *Deep Full-sky Coadds from Three Years of WISE and NEOWISE Observations*, *AJ* **154** (2017) 161 [[1705.06746](#)].
- [38] A. M. Meisner, D. Lang and D. J. Schlegel, *Another unWISE Update: The Deepest Ever Full-sky Maps at 3-5  $\mu\text{m}$* , *Research Notes of the American Astronomical Society* **2** (2018) 1 [[1801.03566](#)].
- [39] E. F. Schlafly, G. M. Green, D. Lang, T. Daylan, D. P. Finkbeiner, A. Lee et al., *The DECam Plane Survey: Optical Photometry of Two Billion Objects in the Southern Galactic Plane*, *The Astrophysical Journal Supplement Series* **234** (2018) 39 [[1710.01309](#)].
- [40] C. Laigle, H. J. McCracken, O. Ilbert, B. C. Hsieh, I. Davidzon, P. Capak et al., *The COSMOS2015 Catalog: Exploring the  $1 < z < 6$  Universe with Half a Million Galaxies*, *ApJS* **224** (2016) 24 [[1604.02350](#)].
- [41] Gaia Collaboration, A. G. A. Brown, A. Vallenari, T. Prusti, J. H. J. de Bruijne, C. Babusiaux et al., *Gaia Data Release 2. Summary of the contents and survey properties*, *A&A* **616** (2018) A1 [[1804.09365](#)].
- [42] D. Makarov, P. Prugniel, N. Terekhova, H. Courtois and I. Vauglin, *HyperLEDA. III. The catalogue of extragalactic distances*, *A&A* **570** (2014) A13 [[1408.3476](#)].
- [43] A. Acker, F. Cuisinier, B. Stenholm and A. Terzan, *New planetary nebulae in the galactic bulge.*, *A&A* **264** (1992) 217.
- [44] D. N. Limber, *The Analysis of Counts of the Extragalactic Nebulae in Terms of a Fluctuating Density Field.*, *ApJ* **117** (1953) 134.
- [45] M. Loverde and N. Afshordi, *Extended Limber approximation*, *PRD* **78** (2008) 123506 [[0809.5112](#)].
- [46] R. Takahashi, M. Sato, T. Nishimichi, A. Taruya and M. Oguri, *Revising the Halofit Model for the Nonlinear Matter Power Spectrum*, *ApJ* **761** (2012) 152 [[1208.2701](#)].
- [47] D. Blas, J. Lesgourgues and T. Tram, *The Cosmic Linear Anisotropy Solving System (CLASS). Part II: Approximation schemes*, *Journal of Cosmology and Astro-Particle Physics* **2011** (2011) 034 [[1104.2933](#)].
- [48] C. Modi, M. White and Z. Vlah, *Modeling CMB lensing cross correlations with CLEFT*, *JCAP* **8** (2017) 009 [[1706.03173](#)].
- [49] M. Costanzi, F. Villaescusa-Navarro, M. Viel, J.-Q. Xia, S. Borgani, E. Castorina et al., *Cosmology with massive neutrinos III: the halo mass function and an application to galaxy clusters*, *Journal of Cosmology and Astro-Particle Physics* **2013** (2013) 012 [[1311.1514](#)].
- [50] F. Villaescusa-Navarro, F. Marulli, M. Viel, E. Branchini, E. Castorina, E. Sefusatti et al., *Cosmology with massive neutrinos I: towards a realistic modeling of the relation between matter, haloes and galaxies*, *Journal of Cosmology and Astro-Particle Physics* **2014** (2014) 011 [[1311.0866](#)].
- [51] E. Castorina, E. Sefusatti, R. K. Sheth, F. Villaescusa-Navarro and M. Viel, *Cosmology with massive neutrinos II: on the universality of the halo mass function and bias*, *Journal of Cosmology and Astro-Particle Physics* **2014** (2014) 049 [[1311.1212](#)].
- [52] E. Castorina, C. Carbone, J. Bel, E. Sefusatti and K. Dolag, *DEMNUi: the clustering of large-scale structures in the presence of massive neutrinos*, *Journal of Cosmology and Astro-Particle Physics* **2015** (2015) 043 [[1505.07148](#)].
- [53] S. Vagnozzi, T. Brinckmann, M. Archidiacono, K. Freese, M. Gerbino, J. Lesgourgues et al., *Bias due to neutrinos must not uncorrect'd go*, *Journal of Cosmology and Astro-Particle Physics* **2018** (2018) 001 [[1807.04672](#)].

- [54] E. Hivon, K. M. Górski, C. B. Netterfield, B. P. Crill, S. Prunet and F. Hansen, *MASTER of the Cosmic Microwave Background Anisotropy Power Spectrum: A Fast Method for Statistical Analysis of Large and Complex Cosmic Microwave Background Data Sets*, *ApJ* **567** (2002) 2 [[astro-ph/0105302](#)].
- [55] D. Alonso, J. Sanchez and A. Slosar, *A unified pseudo- $C_\ell$  framework*, *ArXiv e-prints* (2018) [[1809.09603](#)].
- [56] G. Efstathiou, *Myths and truths concerning estimation of power spectra*, *Mon. Not. Roy. Astron. Soc.* **349** (2004) 603 [[astro-ph/0307515](#)].
- [57] C. García-García, D. Alonso and E. Bellini, *Disconnected pseudo- $C_\ell$  covariances for projected large-scale structure data*, [1906.11765](#).
- [58] J. A. Newman, *Calibrating Redshift Distributions beyond Spectroscopic Limits with Cross-Correlations*, *ApJ* **684** (2008) 88 [[0805.1409](#)].
- [59] M. McQuinn and M. White, *On using angular cross-correlations to determine source redshift distributions*, *MNRAS* **433** (2013) 2857 [[1302.0857](#)].
- [60] B. Ménard, R. Scranton, S. Schmidt, C. Morrison, D. Jeong, T. Budavari et al., *Clustering-based redshift estimation: method and application to data*, *arXiv e-prints* (2013) [[1303.4722](#)].
- [61] H. Aihara, R. Armstrong, S. Bickerton, J. Bosch, J. Coupon, H. Furusawa et al., *First data release of the Hyper Suprime-Cam Subaru Strategic Program*, *PASJ* **70** (2018) S8 [[1702.08449](#)].
- [62] M. Tanaka, J. Coupon, B.-C. Hsieh, S. Mineo, A. J. Nishizawa, J. Speagle et al., *Photometric redshifts for Hyper Suprime-Cam Subaru Strategic Program Data Release 1*, *PASJ* **70** (2018) S9 [[1704.05988](#)].
- [63] S. J. Schmidt, B. Ménard, R. Scranton, C. Morrison and C. K. McBride, *Recovering redshift distributions with cross-correlations: pushing the boundaries*, *MNRAS* **431** (2013) 3307 [[1303.0292](#)].
- [64] S. J. Schmidt, B. Ménard, R. Scranton, C. B. Morrison, M. Rahman and A. M. Hopkins, *Inferring the redshift distribution of the cosmic infrared background*, *MNRAS* **446** (2015) 2696 [[1407.0031](#)].
- [65] M. Rahman, B. Ménard, R. Scranton, S. J. Schmidt and C. B. Morrison, *Clustering-based redshift estimation: comparison to spectroscopic redshifts*, *MNRAS* **447** (2015) 3500 [[1407.7860](#)].
- [66] M. Rahman, A. J. Mendez, B. Ménard, R. Scranton, S. J. Schmidt, C. B. Morrison et al., *Exploring the SDSS photometric galaxies with clustering redshifts*, *MNRAS* **460** (2016) 163 [[1512.03057](#)].
- [67] M. Rahman, B. Ménard and R. Scranton, *Exploring the 2MASS extended and point source catalogues with clustering redshifts*, *MNRAS* **457** (2016) 3912 [[1508.03046](#)].
- [68] V. Scottez, Y. Mellier, B. R. Granett, T. Moutard, M. Kilbinger, M. Scodreggio et al., *Clustering-based redshift estimation: application to VIPERS/CFHTLS*, *MNRAS* **462** (2016) 1683 [[1605.05501](#)].
- [69] V. Scottez, A. Benoit-Lévy, J. Coupon, O. Ilbert and Y. Mellier, *Testing the accuracy of clustering redshifts with simulations*, *MNRAS* **474** (2018) 3921 [[1705.02629](#)].
- [70] A. Johnson, C. Blake, A. Amon, T. Erben, K. Glazebrook, J. Harnois-Deraps et al., *2dFLenS and KiDS: determining source redshift distributions with cross-correlations*, *MNRAS* **465** (2017) 4118 [[1611.07578](#)].

- [71] C. Davis, E. Rozo, A. Roodman, A. Alarcon, R. Cawthon, M. Gatti et al., *Cross-correlation redshift calibration without spectroscopic calibration samples in DES Science Verification Data*, *MNRAS* **477** (2018) 2196 [1707.08256].
- [72] R. Cawthon, C. Davis, M. Gatti, P. Vielzeuf, J. Elvin-Poole, E. Rozo et al., *Dark Energy Survey Year 1 Results: calibration of redMaGiC redshift distributions in DES and SDSS from cross-correlations*, *MNRAS* **481** (2018) 2427 [1712.07298].
- [73] M. Gatti, P. Vielzeuf, C. Davis, R. Cawthon, M. M. Rau, J. DeRose et al., *Dark Energy Survey Year 1 results: cross-correlation redshifts - methods and systematics characterization*, *MNRAS* **477** (2018) 1664 [1709.00992].
- [74] D. J. Bates, R. Tojeiro, J. A. Newman, V. Gonzalez-Perez, J. Comparat, D. P. Schneider et al., *Mass functions, luminosity functions, and completeness measurements from clustering redshifts*, *MNRAS* **486** (2019) 3059 [1810.01767].
- [75] A. J. Mead, J. A. Peacock, C. Heymans, S. Joudaki and A. F. Heavens, *An accurate halo model for fitting non-linear cosmological power spectra and baryonic feedback models*, *MNRAS* **454** (2015) 1958 [1505.07833].
- [76] M. Davis and P. J. E. Peebles, *A survey of galaxy redshifts. V - The two-point position and velocity correlations*, *ApJ* **267** (1983) 465.
- [77] I. Pâris, P. Petitjean, N. P. Ross, A. D. Myers, É. Aubourg, A. Streblyanska et al., *The Sloan Digital Sky Survey Quasar Catalog: Twelfth data release*, *A&A* **597** (2017) A79 [1608.06483].
- [78] M. Ata, F. Baumgarten, J. Bautista, F. Beutler, D. Bizyaev, M. R. Blanton et al., *The clustering of the SDSS-IV extended Baryon Oscillation Spectroscopic Survey DR14 quasar sample: first measurement of baryon acoustic oscillations between redshift 0.8 and 2.2*, *MNRAS* **473** (2018) 4773 [1705.06373].
- [79] B. Reid, S. Ho, N. Padmanabhan, W. J. Percival, J. Tinker, R. Tojeiro et al., *SDSS-III Baryon Oscillation Spectroscopic Survey Data Release 12: galaxy target selection and large-scale structure catalogues*, *MNRAS* **455** (2016) 1553 [1509.06529].
- [80] S. Eftekharzadeh, A. D. Myers, M. White, D. H. Weinberg, D. P. Schneider, Y. Shen et al., *Clustering of intermediate redshift quasars using the final SDSS III-BOSS sample*, *MNRAS* **453** (2015) 2779 [1507.08380].
- [81] J. Bovy, J. F. Hennawi, D. W. Hogg, A. D. Myers, J. A. Kirkpatrick, D. J. Schlegel et al., *Think Outside the Color Box: Probabilistic Target Selection and the SDSS-XDQSO Quasar Targeting Catalog*, *ApJ* **729** (2011) 141 [1011.6392].
- [82] M. White, A. D. Myers, N. P. Ross, D. J. Schlegel, J. F. Hennawi, Y. Shen et al., *The clustering of intermediate-redshift quasars as measured by the Baryon Oscillation Spectroscopic Survey*, *MNRAS* **424** (2012) 933 [1203.5306].
- [83] S. Alam, M. Ata, S. Bailey, F. Beutler, D. Bizyaev, J. A. Blazek et al., *The clustering of galaxies in the completed SDSS-III Baryon Oscillation Spectroscopic Survey: cosmological analysis of the DR12 galaxy sample*, *MNRAS* **470** (2017) 2617 [1607.03155].
- [84] A. J. Ross, F. Beutler, C.-H. Chuang, M. Pellejero-Ibanez, H.-J. Seo, M. Vargas-Magaña et al., *The clustering of galaxies in the completed SDSS-III Baryon Oscillation Spectroscopic Survey: observational systematics and baryon acoustic oscillations in the correlation function*, *MNRAS* **464** (2017) 1168 [1607.03145].
- [85] A. D. Myers, N. Palanque-Delabrouille, A. Prakash, I. Pâris, C. Yeche, K. S. Dawson et al., *The SDSS-IV Extended Baryon Oscillation Spectroscopic Survey: Quasar Target Selection*, *ApJS* **221** (2015) 27 [1508.04472].
- [86] J. M. Loh and M. L. Stein, *Bootstrapping a spatial point process*, *Statistica Sinica* **14** (2004) 69.

- [87] J. M. Loh, *A Valid and Fast Spatial Bootstrap for Correlation Functions*, *ApJ* **681** (2008) 726.
- [88] P. Norberg, C. M. Baugh, E. Gaztañaga and D. J. Croton, *Statistical analysis of galaxy surveys - I. Robust error estimation for two-point clustering statistics*, *MNRAS* **396** (2009) 19 [0810.1885].
- [89] A. D. Myers, P. J. Outram, T. Shanks, B. J. Boyle, S. M. Croom, N. S. Loaring et al., *On statistical lensing and the anticorrelation between 2dF QSOs and foreground galaxies*, *MNRAS* **359** (2005) 741 [astro-ph/0502481].
- [90] N. P. Ross, Y. Shen, M. A. Strauss, D. E. Vanden Berk, A. J. Connolly, G. T. Richards et al., *Clustering of Low-redshift ( $z < 2.2$ ) Quasars from the Sloan Digital Sky Survey*, *ApJ* **697** (2009) 1634 [0903.3230].
- [91] J. N. Fry, *The Evolution of Bias*, *ApJL* **461** (1996) L65.
- [92] P. Laurent, S. Eftekharzadeh, J.-M. Le Goff, A. Myers, E. Burtin, M. White et al., *Clustering of quasars in SDSS-IV eBOSS: study of potential systematics and bias determination*, *JCAP* **7** (2017) 017 [1705.04718].
- [93] P. Craven and G. Wahba, *Smoothing noisy data with spline functions*, *Numer. Math.* **31** (1978) 377.
- [94] S. Ferraro and J. C. Hill, *Bias to CMB Lensing Reconstruction from Temperature Anisotropies due to Large-Scale Galaxy Motions*, *Phys. Rev.* **D97** (2018) 023512 [1705.06751].
- [95] R. G. Kron, *Photometry of a complete sample of faint galaxies.*, *ApJS* **43** (1980) 305.
- [96] O. Le Fèvre, P. Cassata, O. Cucciati, B. Garilli, O. Ilbert, V. Le Brun et al., *The VIMOS VLT Deep Survey final data release: a spectroscopic sample of 35 016 galaxies and AGN out to  $z \sim 6.7$  selected with  $17.5 \leq i_{AB} \leq 24.75$* , *A&A* **559** (2013) A14 [1307.0545].
- [97] C. J. Lonsdale, H. E. Smith, M. Rowan-Robinson, J. Surace, D. Shupe, C. Xu et al., *SWIRE: The SIRTf Wide-Area Infrared Extragalactic Survey*, *Publ. Astron. Soc. Pac.* **115** (2003) 897 [astro-ph/0305375].
- [98] P. Franzetti, M. Scodeggio, B. Garilli, D. Vergani, D. Maccagni, L. Guzzo et al., *The VIMOS-VLT deep survey. Color bimodality and the mix of galaxy populations up to  $z \sim 2$* , *A&A* **465** (2007) 711 [astro-ph/0607075].
- [99] M. J. I. Brown, Z. Zheng, M. White, A. Dey, B. T. Jannuzi, A. J. Benson et al., *Red Galaxy Growth and the Halo Occupation Distribution*, *ApJ* **682** (2008) 937 [0804.2293].
- [100] C. Conroy, R. H. Wechsler and A. V. Kravtsov, *Modeling Luminosity-dependent Galaxy Clustering through Cosmic Time*, *ApJ* **647** (2006) 201 [astro-ph/0512234].
- [101] Z. Zheng, A. A. Berlind, D. H. Weinberg, A. J. Benson, C. M. Baugh, S. Cole et al., *Theoretical Models of the Halo Occupation Distribution: Separating Central and Satellite Galaxies*, *ApJ* **633** (2005) 791 [astro-ph/0408564].
- [102] Planck Collaboration, Y. Akrami, F. Arroja, M. Ashdown, J. Aumont, C. Baccigalupi et al., *Planck 2018 results. I. Overview and the cosmological legacy of Planck*, *ArXiv e-prints* (2018) [1807.06205].
- [103] J. Tinker, A. V. Kravtsov, A. Klypin, K. Abazajian, M. Warren, G. Yepes et al., *Toward a Halo Mass Function for Precision Cosmology: The Limits of Universality*, *ApJ* **688** (2008) 709 [0803.2706].
- [104] J. L. Tinker, B. E. Robertson, A. V. Kravtsov, A. Klypin, M. S. Warren, G. Yepes et al., *The Large-scale Bias of Dark Matter Halos: Numerical Calibration and Model Tests*, *ApJ* **724** (2010) 878 [1001.3162].
- [105] R. K. Sheth and G. Tormen, *Large-scale bias and the peak background split*, *MNRAS* **308** (1999) 119 [astro-ph/9901122].

- [106] R. K. Sheth, H. J. Mo and G. Tormen, *Ellipsoidal collapse and an improved model for the number and spatial distribution of dark matter haloes*, *MNRAS* **323** (2001) 1 [[astro-ph/9907024](#)].
- [107] J. Comparat, F. Prada, G. Yepes and A. Klypin, *Accurate mass and velocity functions of dark matter haloes*, *MNRAS* **469** (2017) 4157 [[1702.01628](#)].
- [108] J. Bovy, A. D. Myers, J. F. Hennawi, D. W. Hogg, R. G. McMahon, D. Schiminovich et al., *Photometric Redshifts and Quasar Probabilities from a Single, Data-driven Generative Model*, *ApJ* **749** (2012) 41 [[1105.3975](#)].
- [109] N. P. Ross, A. D. Myers, E. S. Sheldon, C. Yèche, M. A. Strauss, J. Bovy et al., *The SDSS-III Baryon Oscillation Spectroscopic Survey: Quasar Target Selection for Data Release Nine*, *ApJS* **199** (2012) 3 [[1105.0606](#)].
- [110] M. A. Strauss, D. H. Weinberg, R. H. Lupton, V. K. Narayanan, J. Annis, M. Bernardi et al., *Spectroscopic Target Selection in the Sloan Digital Sky Survey: The Main Galaxy Sample*, *AJ* **124** (2002) 1810 [[astro-ph/0206225](#)].